Communications in Applied Mathematics and Computational Science

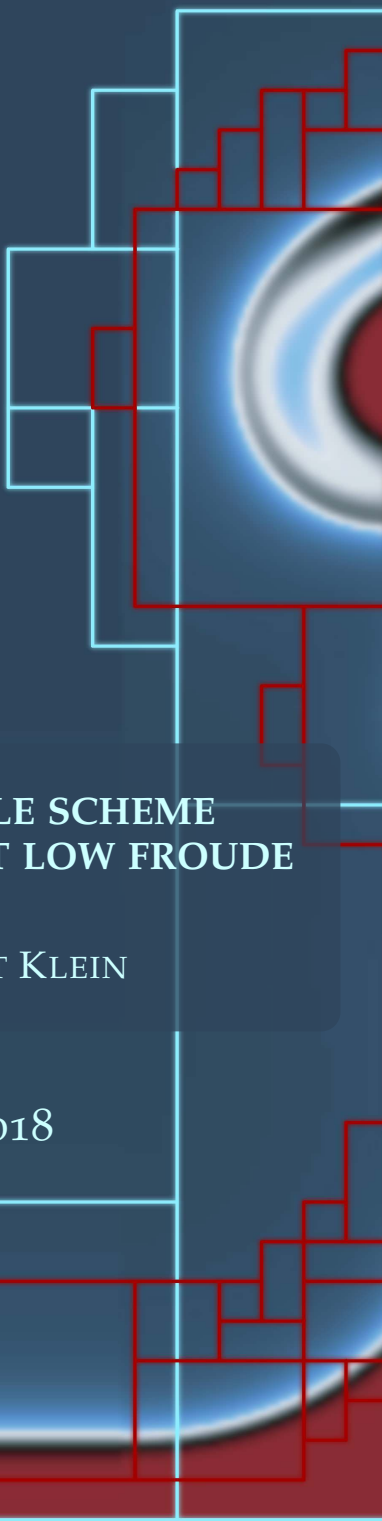

A SEMI-IMPLICIT MULTISCALE SCHEME FOR SHALLOW WATER FLOWS AT LOW FROUDE NUMBER

STEFAN VATER AND RUPERT KLEIN

vol. 13 no. 2 2018

msp

COMM. APP. MATH. AND COMP. SCI.
Vol. 13, No. 2, 2018
dx.doi.org/10.2140/camcos.2018.13.303

A SEMI-IMPLICIT MULTISCALE SCHEME FOR SHALLOW WATER FLOWS AT LOW FROUDE NUMBER

STEFAN VATER AND RUPERT KLEIN

A new large time step semi-implicit multiscale method is presented for the solution of low Froude number shallow water flows. While on small scales which are under-resolved in time the impact of source terms on the divergence of the flow is essentially balanced, on large resolved scales the scheme propagates free gravity waves with minimized diffusion. The scheme features a scale decomposition based on multigrid ideas. Two different time integrators are blended at each scale depending on the scale-dependent Courant number for gravity wave propagation. The finite volume discretization is implemented in the framework of second-order Godunov-type methods for conservation laws. The basic properties of the method are validated by numerical tests. This development is a further step in the construction of asymptotically adaptive numerical methods for the computation of large-scale atmospheric flows.

1. Introduction

Modern high-performance computing hardware allows for high-resolution atmospheric flow simulations, which resolve scales ranging from small convective-scale essentially anelastic flows up to large planetary-scale dynamics (see, e.g., [32]). Such simulations are not only demanding in terms of problem size. They also challenge the applied numerical methods, which must correctly resolve the different characteristic flow regimes arising on the different scales captured by the discretization.

An example is the influence of sound waves and the associated compressibility. These waves are usually considered to have little influence in meteorological applications, because the much slower synoptic and planetary wave patterns associated with inertia and advection are most relevant for predicting the weather. This led to so-called approximate "sound-proof" model equations [31; 28; 1; 9], which do not include the fast acoustic waves and have been quite popular to model small-scale atmospheric dynamics. The situation is different for planetary-scale

MSC2010: 65M08, 86A10.
Keywords: shallow water equations, multiscale time integration, asymptotically adaptive numerical methods, large time steps, balanced modes.

dynamics, where long-wave horizontally traveling acoustic modes, i.e., Lamb waves, are sometimes considered nonnegligible. Furthermore, there are indications that effects of compressibility affect large-scale, deep internal wave modes of the atmosphere in a nontrivial fashion [7]. These dynamics are fairly captured by another reduced model, namely the hydrostatic primitive equations (HPEs), which are widely used in current operational general circulation models. At resolutions of only a few kilometers, however, the HPEs loose their validity due to the breakdown of the hydrostatic assumption. Therefore, at least for an accurate representation of large-scale planetary-scale dynamics, the challenge arises of combining large-scale compressible flow representations with essentially sound-proof modeling of the small-scale dynamics.

For the mathematical study of interactions across scales, techniques from multiple-scales asymptotics [16; 22] are increasingly used. These are extensions of the classical single-scale asymptotic method (also known as regular perturbation analysis). In the latter, a small nondimensional parameter of the problem and a special (asymptotic) expansion of the dependent variables are employed to obtain simplified equation sets, which still account for the physical effects characteristic to the specific scale. Examples are the aforementioned anelastic and hydrostatic approximations. In multiple-scales asymptotic analysis the asymptotic expansion is generalized in that the variables artificially depend on more than one space or time scale. This enables the study of effects arising across scales. Since the asymptotic analysis directly relates a reduced model to the full compressible flow equations, it is a natural starting point for the development of numerical methods applicable to the considered singular regimes [20; 22]. In this context, the notion of "asymptotically adaptive numerical methods" was suggested in [18; 19; 24]. Such schemes should be robust, uniformly accurate, and efficient in the vicinity of certain asymptotic regimes and over a variety of relevant applications. The idea is closely related to "asymptotic preserving" schemes (see [5] and references therein).

The aim of this work is to develop such an asymptotically adaptive numerical method that is able to correctly simulate large-scale compressible flow phenomena with high resolution. In this initial attempt not the full dynamics of the atmosphere are considered. Instead, this work deals with the shallow water equations, which describe the vertically averaged motion of an incompressible fluid with a free surface. By "shallow" one refers to the small aspect ratio between the vertical depth and a typical horizontal length scale of the problem, which justifies the hydrostatic assumption, i.e., that the pressure balances the weight of the fluid. However, these equations are not only a good model for representing river flow or large-scale oceanic motions (such as tsunamis). While ignoring the presence of stratification, the shallow water equations incorporate the effects of gravity and can account for the Earth's rotation and for bottom topography by the addition of appropriate

source terms. Therefore, they are prototypical of the hydrostatic primitive equations and are often used in the development of numerical methods for atmospheric flow problems.

Due to the vertical averaging of the prognostic variables, the shallow water equations only admit external waves. However, the external gravity waves in shallow water flows are the equivalent to Lamb waves in the compressible flow equations [15]. The considered asymptotic regime consists of long-wave acoustic waves (Lamb waves) interacting with slow advection. This is equivalent to the regime of fast gravity waves moving over short-range topography in the shallow water context. The additional atmospheric effect of small-scale flow divergence induced by local diabatic sources is modeled here by a time-dependent bottom topography. Such effects are important when incorporating moist atmospheric processes, such as condensation and rain. In this context, the shallow water model represents a challenging part of the development of numerical methods for the simulation of planetary-scale atmospheric flows at high resolution.

The analysis of the regime of fast gravity waves moving over short-range topography reveals that it essentially consists of long-wave linearized shallow water flow interacting with small-scale flow balancing the influence of the rough topography (see Section 2 for details and [4] by Bresch et al.). Therefore, the new scheme should

- eliminate freely propagating "compressible" short-wave modes that it cannot represent accurately due to temporal under-resolution,
- represent with second-order accuracy the "slaved" dynamics of short-wave solution components induced by slow forcing or arising in the form of high-order corrections to long-wave modes, and
- minimize numerical dispersion for resolved modes.

The first and last points address the specific numerical dispersion behavior of common second-order implicit time discretizations, which usually slow down modes with high wavenumbers [43; 10]. While the decision which modes can be considered to be resolved is certainly subjective and depends on the application, at some point the slowdown of modes with wavenumbers larger than a certain value is unacceptable. These modes should be eliminated over time in a consistent way. On the other hand, long-wave modes, whose oscillation is well resolved at a fixed position, should be well approximated. The second point refers to the balanced flow on the small scale of the regime, which depends on local source terms and the coupling to the large-scale dynamics.

To achieve these goals, a semi-implicit method for the nonlinear shallow water equations is combined with a multilevel approach which has successfully been applied to the linearized equations to model multiscale behavior in [43]. The latter enables the association of different solution components with certain spatial scales

and is based on geometric multigrid ideas. Furthermore, selective to each scale, a proper discretization is applied. The approach results in a robust representation of balanced, slowly forced fast modes on the one hand, and a proper propagation of long-wave gravity waves on the other hand.

The present work extends ideas of multiscale time integration for compressible flows formulated earlier in [18; 12; 30]. These authors already suggested separating the short- and long-wave components of a flow field and to propagate these components in time by different time integration schemes. However, they only allowed for two distinct discrete scales: one representing small-scale solution components and one for long-wave acoustic modes, which are separated from each other by a factor of $1/\mathsf{M}$, where M is the Mach number. In contrast, by introducing multigrid decompositions of the flow and a smooth blending of time integrators, we obtain a scheme in this work that allows for much more general data with true multiscale content. Our work extends that of [43] from linear wave propagation in one space dimension to the nonlinear shallow water equations.

This article is structured into the following parts. After the presentation of the governing equations we discuss the asymptotic regime of interest in the next section. The multiscale scheme is then described by a semidiscretization in time in Section 3. In this course, we first extend a zero Froude number projection method to nonzero Froude numbers. The multilevel approach is included in the implicit correction step, which accounts for the correct propagation of gravity waves. Finally, we show the correct behavior of the method by some one-dimensional test cases in Section 4 and give conclusions in Section 5.

2. Governing equations

The derivation of the shallow water equations can be found in numerous textbooks (see, e.g., [34; 38]). The case of nonstationary bottom topography was dealt with in [41]. Here, only the resulting equations are presented and the peculiarities concerning time-dependent bottom topography are pointed out. Furthermore, the governing equations are analyzed in the limit of a small Froude number. Particularly, the asymptotic limit regime for long-wave shallow water waves passing over short-range topography as presented in [4] is discussed under the additional assumption of bottom topography changing in time.

2.1. ***Shallow water flows with time-dependent bottom topography.*** The assumption of a time-dependent bottom topography, which is slightly unusual, is considered to model a source term which acts on the local flow divergence as outlined in the introduction. This generalization neither changes the terms arising in the shallow water equations nor does it introduce additional ones. Therefore, the governing

equations in conservation form are given by

$$\begin{aligned} h_t + \nabla \cdot (h\boldsymbol{u}) &= 0, \\ (h\boldsymbol{u})_t + \nabla \cdot (h\boldsymbol{u} \circ \boldsymbol{u}) + \frac{1}{2\mathsf{Fr}^2}\nabla(h^2) &= -\frac{1}{\mathsf{Fr}^2} h \nabla b. \end{aligned} \tag{1}$$

Here, $h(t, \boldsymbol{x})$ is the thickness or depth of the fluid and $\boldsymbol{u}(t, \boldsymbol{x})$ its depth-averaged horizontal velocity, and $b(t, \boldsymbol{x})$ denotes the time- and space-dependent bottom topography. The gradient operator ∇ is acting in the horizontal $\boldsymbol{x} = (x, y)$ plane. The "$\circ$" denotes the dyadic product of two vectors. A temporal change in bottom topography either changes the total height $H = h + b$ or introduces divergence in the momentum field, as can be seen from reformulating the continuity equation to

$$H_t + \nabla \cdot (h\boldsymbol{u}) = b_t. \tag{2}$$

Furthermore, a change in the gradient of b directly enters the source term of the momentum equation, leading to a potential disruption of the hydrostatic equilibrium of a previously balanced flow. System (1) is given in nondimensional form introducing the dimensionless characteristic quantity $\mathsf{Fr} := v_{\text{ref}}/\sqrt{g h_{\text{ref}}}$, which is known as the Froude number. It defines the ratio between the characteristic flow velocity v_{ref} and the gravity wave speed $\sqrt{g h_{\text{ref}}}$ with g being the acceleration due to gravity and h_{ref} a reference fluid depth. Since we are interested in phenomena associated with the advective time scale of the fluid, we set $t_{\text{ref}} = \ell_{\text{ref}}/v_{\text{ref}}$ in the dimensional analysis and omitted mentioning of the Strouhal number.

The shallow water equations are mathematically equivalent to the Euler equations of compressible isentropic gas dynamics for an isentropic exponent of $\gamma = 2$. In this respect, the Froude number in the shallow water equations takes the role of the Mach number in the Euler equations, the latter being a measure of the compressibility of the fluid. Therefore, effects similar to compressibility can also be modeled by the shallow water equations, where the importance of the "compressibility" depends on the associated scales of fluid motion. In large scale atmospheric applications, a typical flow velocity is 10 m/s and the depth of the atmosphere is given by the pressure scale height, which is approximately 10 km. This results in a Froude number $\mathsf{Fr} \approx 0.03 \ll 1$, and the "compressibility" effects associated with the nonlinear nature of external gravity waves plays a minor role in this regime. Note, however, that the shallow water equations intrinsically model an incompressible fluid.

2.2. ***Long-wave gravity waves passing over short-range topography.*** The regime of particular interest can be characterized by long-wave shallow water waves traveling over rough topography. Consider a multiple-space-scale/single-time-scale analysis for this regime akin to [18; 4; 25]. In addition to the space coordinate $\boldsymbol{x}$ defined by nondimensionalization with the reference length ℓ_{ref}, a second large-scale coordinate $\boldsymbol{\xi} = \mathsf{Fr}\boldsymbol{x}$ is introduced, which resolves the distance a gravity wave

traverses on the considered time scale. For the bottom topography $b = b(t, \boldsymbol{x}, \boldsymbol{\xi})$ we allow for variations on both space scales. Then, the fluid depth and velocity are expressed in the multiple-scales expansion

$$(h, \boldsymbol{u})(t, \boldsymbol{x}; \mathsf{Fr}) = \sum_{i=0}^{N} \mathsf{Fr}^i (h, \boldsymbol{u})^{(i)}(t, \boldsymbol{x}, \boldsymbol{\xi}) + \mathcal{O}(\mathsf{Fr}^N). \tag{3}$$

Note that, by using this ansatz, each spatial derivative of an asymptotic function $\varphi^{(i)}$ translates into

$$\nabla \varphi^{(i)}|_{\mathsf{Fr}} = \nabla_{\boldsymbol{x}} \varphi^{(i)} + \mathsf{Fr} \nabla_{\boldsymbol{\xi}} \varphi^{(i)} \tag{4}$$

for fixed Froude number Fr. As stated above, this regime has also been discussed in [4] but without time-dependent bottom topography. The leading-order system is separated into two subsystems representing the long-wave and the short-wave components of the flow. They are given by the *long-wave equations for rough topography*

$$\begin{aligned} \overline{(h\boldsymbol{u})^{(0)}}_t + \overline{h^{(0)}} \nabla_{\boldsymbol{\xi}} h^{(1)} &= \overline{h^{(2)} \nabla_{\boldsymbol{x}} h^{(0)}}, \\ h^{(1)}_t + \nabla_{\boldsymbol{\xi}} \cdot \overline{(h\boldsymbol{u})^{(0)}} &= 0 \end{aligned} \tag{5}$$

and the associated *balanced small-scale flow*

$$\begin{aligned} \tilde{\tilde{\tilde{\tilde{(h\boldsymbol{u})^{(0)}}}}}_t + \nabla_{\boldsymbol{x}} \cdot (h\boldsymbol{u} \circ \boldsymbol{u})^{(0)} + \tilde{\tilde{\tilde{\tilde{h^{(0)} \nabla_{\boldsymbol{x}} h^{(2)}}}}} &= -\tilde{\tilde{\tilde{h^{(0)}}}} \nabla_{\boldsymbol{\xi}} h^{(1)}, \\ \nabla_{\boldsymbol{x}} \cdot (h\boldsymbol{u})^{(0)} = \nabla_{\boldsymbol{x}} \cdot \tilde{\tilde{\tilde{\tilde{(h\boldsymbol{u})^{(0)}}}}} &= \tilde{b}_t. \end{aligned} \tag{6}$$

The leading-order fluid depth is given by

$$h^{(0)}(t, \boldsymbol{x}, \boldsymbol{\xi}) = H^{(0)}(t) - b(t, \boldsymbol{x}, \boldsymbol{\xi}),$$

where $H^{(0)}$ is the leading-order surface elevation of the fluid and $dH^{(0)}/dt = \bar{b}_t$. The next order of the fluid depth $h^{(1)} = h_1(t, \boldsymbol{\xi})$ is independent of $\boldsymbol{x}$. Here the overbar denotes the average of the pertinent variable in the fast coordinate, $\boldsymbol{x}$, and the wiggly overline indicates the zero-average remainder or fluctuation.

Compared to the linear case (cf. [41]) the two systems (5) and (6) are coupled. The large-scale flow is given by the linearized shallow water equations, which involve nonbalanced free surface waves. It is driven by a source term arising from the small-scale flow in the momentum equation. This source represents the accumulated pressure force, which results from the small-scale flow across the rough topography. In the opposite direction, large-scale gradients of the fluid depth acting on the rough topography induce small-scale momentum. This modifies the otherwise balanced small-scale flow.

In contrast to [4] a source term acting on the local divergence of the flow arises, when considering nonstationary bottom topography. It is generated by local variations in time of the bottom topography. Furthermore, the changes of the mean

in b over time induce a change in the leading-order surface elevation $H^{(0)}$, and the signal speed of the long-wave gravity waves is changing not only in space, but also in time.

Similar asymptotic regimes were studied in [18] concerning weakly compressible flows with small-scale entropy and vorticity, in [26] for modeling ocean flows, and in the context of atmospheric circulation near the equator in [29].

The asymptotic scaling for the velocity in this regime is given by $\boldsymbol{u} \sim 1$ as $\mathsf{Fr} \to 0$. For the fluid depth we have $h - h_0(t) \sim \mathsf{Fr}$ on the large scale and $h - h_0(t) \sim \mathsf{Fr}^2$ on the small scale. This scaling should be reproduced by a numerical scheme, especially when $\Delta t \gg \Delta\xi/\sqrt{H_0} = \mathsf{Fr}\Delta x/\sqrt{H_0}$, the latter corresponding to large Courant numbers with respect to gravity waves for the time integration in the present model problem.

2.3. ***From zero to low Froude numbers.*** To be able to extend the numerical machinery known from projection methods applied to the zero Froude number shallow water equations (also known as "Lake equations"), the shallow water equations must be cast into a similar form. To reformulate system (1), let us decompose the fluid depth into

$$h(t, \boldsymbol{x}; \mathsf{Fr}) = h_0(t, \boldsymbol{x}) + \mathsf{Fr}^2 h'(t, \boldsymbol{x}) \tag{7}$$

with

$$h_0(t, \boldsymbol{x}) = H_0(t) - b(t, \boldsymbol{x}). \tag{8}$$

Here, H_0 is the mean background total elevation, which can only change due to flow over the boundary of the domain or to a change in the mean bottom topography. Therefore, h_0 can only change due to boundary flow or (local) change of bottom topography. The dynamics of the flow are thus given by the perturbation h' of the fluid depth. This ansatz is justified by the asymptotic analysis of the zero Froude number limit of the governing equations, and we expect that $h' = \mathcal{O}(1)$ as $\mathsf{Fr} \to 0$ in the flow regimes of interest. Inserting this into the governing system, the shallow water equations can be rewritten as

$$\begin{aligned} h_t + \nabla \cdot (h\boldsymbol{u}) &= 0, \\ (h\boldsymbol{u})_t + \nabla \cdot (h\boldsymbol{u} \circ \boldsymbol{u}) + h\nabla h' &= 0, \\ h &= h_0 + \mathsf{Fr}^2 h'. \end{aligned} \tag{9}$$

Compared to the zero Froude number equations, h' takes the role of $h^{(2)}$, but is no longer a Lagrange multiplier. Therefore, also the velocity no longer satisfies a strict divergence constraint. However, at low Froude numbers, these fields should be close to their zero Froude number counterparts. This is due to the mathematical equivalence of the shallow water and the Euler equations and related convergence results for the low Mach number limit of the Euler equations (see, e.g., [17]).

3. Numerical scheme

The numerical scheme to correctly capture the multiscale behavior of the flow is based on a semi-implicit discretization of the shallow water equations, the latter being an extension of a zero Froude number projection method as in [42]. This construction ensures that the discretization correctly approximates the limit behavior of the equations. A second ingredient is a scale-selective multilevel scheme which was previously derived for the linearized equations [43; 41]. With this addition we account for the characteristic flow behavior on the different scales resolved by the discretization.

The semi-implicit method consists of a predictor step, which solves an auxiliary hyperbolic system. This is followed by a first elliptic correction to adjust the advective flux components. A second elliptic correction accounts for the accurate propagation of gravity waves. This is where we incorporate the multilevel scheme for linearized flows. The multilevel scheme is based on two different time discretizations. A scalewise decomposition of the flow information based on geometric multigrid ideas enables a scale-dependent blending of the two time discretizations. Here, we employ the implicit midpoint rule and the BDF(2) scheme, which are both second-order accurate and need the solution of only one linear system. The implicit midpoint rule conserves energy of all wave modes. While this is advantageous for long waves, it is not desirable for high-wavenumber modes, due to the unfavorable discrete dispersion relation. Backward differentiation (BDF) schemes, on the other hand, are able to filter these short-wave modes in a consistent way. In the present work, only uniform time steps are considered. This simplifies the application of multistep methods, since it is not required to account for the different time step sizes. Often these methods can be generalized to variable time steps as in the case of BDF(2) [8].

Similar to the formulation of a zero Froude number projection method as in [42], the semi-implicit scheme is derived by a semidiscretization in time. The discretization in space is discussed in a second step. The essential difference from the zero Froude number case is that the ansatz (7) for the fluid depth involves the introduction of local time derivatives of this quantity. This leads to the solution of two Helmholtz problems in the correction steps.

3.1. ***Explicit predictor and advective flux correction.*** The auxiliary system solved in the predictor step is given by

$$\begin{aligned} h_t + \nabla \cdot (h\boldsymbol{u}) &= 0, \\ (h\boldsymbol{u})_t + \nabla \cdot (h\boldsymbol{u} \circ \boldsymbol{u}) &= -(h \nabla h')^{\mathrm{old}}, \end{aligned} \tag{10}$$

where the right-hand side of the momentum equation is treated as a "source term" and computed from an old (known) time level. The homogeneous part of (10) is known as the "pressureless equations" (see [2; 3; 27] and references therein).

The source term is set to $(h\nabla h')^{\text{old}}(\boldsymbol{x}) := (h\nabla h')(t^n, \boldsymbol{x})$, where $h'^{,n}$ is computed from h^n by using (7), i.e.,

$$h'^{,n} = \frac{1}{\mathsf{Fr}^2}(h^n - H_0^n + b^n). \tag{11}$$

Here and in the following $h(\boldsymbol{x}, t^n)$ is abbreviated by h^n, etc.

Integrating the governing equations from time level t^n to $t^{n+1} := t^n + \Delta t$ and using the midpoint rule by evaluating the flux terms at the half time levels $t^{n+1/2} := t^n + \Delta t/2$ yields

$$h^{n+1} = h^n - \Delta t[\nabla \cdot (h\boldsymbol{u})^{n+1/2}] \tag{12}$$

and

$$(h\boldsymbol{u})^{n+1} = (h\boldsymbol{u})^n - \Delta t[\nabla \cdot (h\boldsymbol{u} \circ \boldsymbol{u})^{n+1/2} + (h\nabla h')^{n+1/2}], \tag{13}$$

which is second-order accurate. To obtain an accurate and stable approximation of the advective flux terms, the momentum $(h\boldsymbol{u})^{*,n+1/2}$ computed by the auxiliary system is modified by a height correction $\delta h'^{,n}_{\text{fl}}$ (where the subscript "fl" refers to the fact that this is a correction to the advective flux components):

$$(h\boldsymbol{u})^{n+1/2} = (h\boldsymbol{u})^{*,n+1/2} - \frac{\Delta t}{2} h^n \nabla \delta h'^{,n}_{\text{fl}}. \tag{14}$$

Applying the divergence to this equation in combination with the height update (12) leads to an (uncritical) Helmholtz problem for $\delta h'^{,n}_{\text{fl}}$:

$$-\frac{\mathsf{Fr}^2}{\Delta t}\delta h'^{,n}_{\text{fl}} + \frac{\Delta t}{2}\nabla \cdot (h^n \nabla \delta h'^{,n}_{\text{fl}}) = \frac{H_0^{n+1} - H_0^n}{\Delta t} - \frac{b^{n+1} - b^n}{\Delta t} - \frac{h^{*,n+1} - h^n}{\Delta t}. \tag{15}$$

The last term on the right-hand side is obtained by substituting the divergence of the auxiliary momentum through the height equation of (10). Note that for $\mathsf{Fr} = 0$ this equation becomes identical to the first correction of a projection method as in [42]. Using (14), the height at the new time level as given in (12) and the advective components of the momentum flux can be computed.

As written above, for the multiscale method we employ two different time discretizations to correct the remaining nonconvective flux component $(h\nabla h')^n$ in the momentum equation. The first is based on the implicit midpoint rule as given in (13). By the definition of

$$(h\boldsymbol{u})^{**}_{\text{IMP}} := (h\boldsymbol{u})^n - \Delta t[\nabla \cdot (h\boldsymbol{u} \circ \boldsymbol{u})^{n+1/2} + (h\nabla h')^n], \tag{16}$$

(the subscript "IMP" referring to the implicit midpoint rule) the momentum at the new time level is obtained by

$$(h\boldsymbol{u})^{n+1} = (h\boldsymbol{u})^{**}_{\text{IMP}} - \frac{\Delta t}{2}(\delta h^n \nabla h'^{,n} + h^{n+1/2}\nabla \delta h'^{,n}), \tag{17}$$

where $\delta h^n := h^{n+1} - h^n$ and $h^{n+1/2} := \frac{1}{2}(h^n + h^{n+1})$. Here $\delta h'^{,n} := h'^{,n+1} - h'^{,n}$ is the update for the perturbation of the fluid depth computed in the second correction.

The second time discretization utilizes the BDF(2) scheme, where the momentum equation is discretized by

$$(h\boldsymbol{u})^{n+1} = \tfrac{4}{3}(h\boldsymbol{u})^n - \tfrac{1}{3}(h\boldsymbol{u})^{n-1} - \frac{2\Delta t}{3}[\nabla \cdot (h\boldsymbol{u} \circ \boldsymbol{u})^{n+1} + (h\nabla h')^{n+1}]. \tag{18}$$

Note that the advective flux component $\nabla \cdot (h\boldsymbol{u} \circ \boldsymbol{u})$ is only available at the half time level from the predictor and first correction. Since for the BDF discretization this term is needed at the full time level t^{n+1}, it is linearly extrapolated from older time levels by

$$(h\boldsymbol{u} \circ \boldsymbol{u})^{n+1} := (h\boldsymbol{u} \circ \boldsymbol{u})^{n+1/2} + \tfrac{1}{2}((h\boldsymbol{u} \circ \boldsymbol{u})^{n+1/2} - (h\boldsymbol{u} \circ \boldsymbol{u})^{n-1/2}). \tag{19}$$

A resulting intermediate momentum update is then given by

$$(h\boldsymbol{u})^{**}_{\mathrm{BDF2}} := \tfrac{4}{3}(h\boldsymbol{u})^n - \tfrac{1}{3}(h\boldsymbol{u})^{n-1} - \frac{2\Delta t}{3}[\nabla \cdot (h\boldsymbol{u} \circ \boldsymbol{u})^{n+1} + (h\nabla h')^n], \tag{20}$$

and the momentum at the new time level is computed by

$$(h\boldsymbol{u})^{n+1} = (h\boldsymbol{u})^{**}_{\mathrm{BDF2}} - \frac{2\Delta t}{3}(\delta h^n \nabla h'^{,n} + h^{n+1}\nabla \delta h'^{,n}). \tag{21}$$

3.2. ***Second correction.*** For the computation of $\delta h'^{,n}$ the final momentum updates (17) and (21) are combined with a corresponding discretization of the height equation. Using the implicit midpoint rule and further interpolation of the half time level value by the full time level values yields

$$\nabla \cdot \frac{(h\boldsymbol{u})^{n+1} + (h\boldsymbol{u})^n}{2} = -\frac{h^{n+1} - h^n}{\Delta t}. \tag{22}$$

By substitution of (17) into this equation, we obtain an (uncritical) Helmholtz problem for the height update $\delta h'^{,n}$

$$-\frac{2\mathsf{Fr}^2}{\Delta t}\delta h'^{,n} + \frac{\Delta t}{2}\nabla \cdot (\hat{h}^{n+1/2}\nabla \delta h'^{,n}) = 2\frac{H_0^{n+1} - H_0^n}{\Delta t} - 2\frac{b^{n+1} - b^n}{\Delta t} + \nabla \cdot (h\boldsymbol{u})^n + \nabla \cdot (h\boldsymbol{u})^{**}_{\mathrm{IMP}} - \frac{\Delta t}{2}\nabla \cdot (\widehat{\delta h}^n \nabla h'^{,n}). \tag{23}$$

Apart from the last term on the right-hand side, for $\mathsf{Fr} = 0$ this equation is again essentially equivalent to the zero Froude number case. In the case of the zero Froude number projection method, this last term (without the hat over δh^n) appears in the intermediate momentum update, since there the height update is given through $H_0(t)$ and $b(t, \boldsymbol{x})$. In the low Froude number case, however, we have $\delta h^n = \delta H_0^n + \mathsf{Fr}^2 \delta h'^{,n}$,

which means that actually the part $\mathrm{Fr}^2\Delta t/2\nabla\cdot(\delta h'^{,n}\nabla h'^{,n})$ should be on the left-hand side of the equation, modifying the solution operator. This issue is solved by using the height update known from the first correction (denoted by the hat), i.e.,

$$\widehat{\delta h}^n := (h^{*,n+1} - h^n) + \frac{\Delta t^2}{2}\nabla\cdot(h^n\nabla\delta h'^{,n}_{\mathrm{fl}}), \tag{24}$$

to compute this term. The same is true for the weight of the Laplacian in the Helmholtz operator on the left-hand side, where we also apply the height obtained from the first correction. Note that this does not modify the final momentum update (17), where the solution $\delta h'^{,n}$ of (23) must be used to determine δh^n in order to get conservation of momentum in the absence of nontrivial bottom topography.

To obtain a BDF(2)-type discretization of the second correction, the height equation is discretized by

$$h^{n+1} = \tfrac{4}{3}h^n - \tfrac{1}{3}h^{n-1} - \frac{2\Delta t}{3}[\nabla\cdot(h\boldsymbol{u})^{n+1}]. \tag{25}$$

Similarly to the discretization using the implicit midpoint rule, the momentum update (21) is then combined with (25) to obtain an equation for $\delta h'^{,n}$. This leads to the (uncritical) Helmholtz problem

$$-\frac{3\mathrm{Fr}^2}{2\Delta t}\delta h'^{,n} + \frac{2\Delta t}{3}\nabla\cdot(\hat{h}^{n+1}\nabla\delta h'^{,n}) = -\frac{\mathrm{Fr}^2}{2\Delta t}\delta h'^{,n-1} + \frac{3h_0^{n+1} - 4h_0^n + h_0^{n-1}}{2\Delta t} + \nabla\cdot(h\boldsymbol{u})^{**}_{\mathrm{BDF2}} - \frac{2\Delta t}{3}\nabla\cdot(\widehat{\delta h}^n\nabla h'^{,n}), \tag{26}$$

where $h_0^n = H_0^n - b^n$. Here again, the values with the hats are approximations obtained from the height computed in the first correction. To conserve momentum in the absence of nontrivial bottom topography, also in this case the result of (26) must be used in the final momentum update (21) for the calculation of δh^n and h^{n+1}.

In addition to the two schemes described above, we consider the so-called θ-scheme. This means that the nonconvective flux term $(h\nabla h')^{n+\theta}$ in (13) is approximated at $t^n + \theta\Delta t$, and (22) is substituted by

$$\theta\nabla\cdot(h\boldsymbol{u})^{n+1} + (1-\theta)\nabla\cdot(h\boldsymbol{u})^n = -\frac{h^{n+1} - h^n}{\Delta t}, \quad \theta\in[0,1]. \tag{27}$$

For $\theta = 1$, this method becomes the implicit Euler method. While it is of second-order accuracy only for $\theta = 0.5$ (equivalent to the implicit midpoint rule), the scheme usually stabilizes for $\theta \in (0.5, 1]$, since more numerical diffusion is introduced.

3.3. ***Multiscale scheme.*** With the introduction of the implicit midpoint and the BDF(2)-based time discretizations for the second correction, all ingredients are now at hand to apply the multilevel scheme from [43] as part of a semi-implicit

method to the fully nonlinear shallow water equations. The idea is to define direct scale-dependent splittings of the fields for fluid depth and momentum, i.e.,

$$\delta h' = \sum_{\nu=0}^{\nu_M} \delta h'^{,(\nu)} \quad \text{and} \quad (h\boldsymbol{u}) = \sum_{\nu=0}^{\nu_M} (h\boldsymbol{u})^{(\nu)}. \tag{28}$$

Ideally, this could be a quasispectral or wavelet decomposition, splitting the discrete fields into (local) high-wavenumber and low-wavenumber components. Each scale component should be treated depending on how well it is resolved by the underlying implicit time discretization. For each scale ν we introduce a blending parameter μ_ν, which depends on the grid CFL number associated to the scale. It is designed such that for well resolved scales the implicit midpoint rule is used, while for scales which are under-resolved in time it blends towards the BDF(2) scheme.

Since we do not want to solve for separate corrections on each scale, we carefully analyze the formal contribution of the two different time discretizations on each scale. With this information and the application of multigrid prolongation and restriction operators, we derive a multilevel elliptic problem, which yields the correction for our semi-implicit discretization.

By the introduction of projection operators Π_ν^h and $\Pi_\nu^{(h\boldsymbol{u})}$, which project a height or momentum field to the scale ν, the contribution for each scale shall be given by

$$\delta h'^{,(\nu)} = (\Pi_\nu^h - \Pi_{\nu-1}^h)\delta h' \quad \text{and} \quad (h\boldsymbol{u})^{(\nu)} = (\Pi_\nu^{(h\boldsymbol{u})} - \Pi_{\nu-1}^{(h\boldsymbol{u})})(h\boldsymbol{u}), \tag{29}$$

where we set $\Pi_{-1}^h \equiv 0$ and $\Pi_{-1}^{(h\boldsymbol{u})} \equiv 0$ for simplicity. The scalewise contribution, which results from blending of the schemes, is then defined as follows. With the application of the two schemes for the semi-implicit solution of the shallow water equations, two different intermediate momentum updates are available after the first correction. For the implicit midpoint time discretization this is (16), whereas for the BDF(2)-based discretization the update is given by (20). With these updates, the right-hand sides of the second correction equations (23) and (26) are given by

$$f_{\mathrm{IMP}}^{\delta h'} = -\frac{2}{\Delta t}\left[2\frac{h_0^{n+1} - h_0^n}{\Delta t} + \nabla\cdot(h\boldsymbol{u})^n + \nabla\cdot(h\boldsymbol{u})_{\mathrm{IMP}}^{**} - \frac{\Delta t}{2}\nabla\cdot(\widehat{\delta h}^n \nabla h'^{,n})\right] \tag{30}$$

and

$$f_{\mathrm{BDF2}}^{\delta h'} = \frac{3\mathsf{Fr}^2}{4\Delta t^2}\delta h'^{,n-1} - \frac{3}{2\Delta t}\left[\frac{3h_0^{n+1} - 4h_0^n + h_0^{n-1}}{2\Delta t} + \nabla\cdot(h\boldsymbol{u})_{\mathrm{BDF2}}^{**} - \frac{2\Delta t}{3}\nabla\cdot(\widehat{\delta h}^n \nabla h'^{,n})\right]. \tag{31}$$

Here, both correction equations have been normalized, such that the weighted Laplacian is essentially the same in the two resulting Helmholtz operators. Note that

this choice is somehow arbitrary and one could have chosen another normalization. For example in [43] we used a normalization where the terms without derivatives in the Helmholtz operators have the common weight 1. Further analysis revealed, however, that this choice can introduce spurious kinks into the solution for the momentum variable. The Helmholtz operators are then given by

$$A_{\mathrm{IMP}} = \frac{4\mathsf{Fr}^2}{\Delta t^2}\,\mathrm{id} - \nabla\cdot(\hat{h}^{n+1/2}\nabla) \quad \text{and} \quad A_{\mathrm{BDF2}} = \frac{9\mathsf{Fr}^2}{4\Delta t^2}\,\mathrm{id} - \nabla\cdot(\hat{h}^{n+1/2}\nabla), \tag{32}$$

where the "id" stands for the identity operator. Note that here we also modified the weight in the Laplacian of the operator for the BDF(2) scheme from $\hat{h}^{n+1}$ to $\hat{h}^{n+1/2}$. Using the projections from (29), a scalewise application and summation over the scales results in a multiscale operator, which is given by

$$A := \sum_{\nu=0}^{\nu_M} (\mu_\nu A_{\mathrm{IMP}} + (1-\mu_\nu) A_{\mathrm{BDF2}})(\Pi_\nu^h - \Pi_{\nu-1}^h) \tag{33}$$

or, in particular for the operators defined in (32),

$$A := \frac{\mathsf{Fr}^2}{\Delta t^2}\left[\sum_{\nu=0}^{\nu_M} (4\mu_\nu + \tfrac{9}{4}(1-\mu_\nu))(\Pi_\nu^h - \Pi_{\nu-1}^h)\right] - \nabla\cdot(\hat{h}^{n+1/2}\nabla). \tag{34}$$

With this operator the elliptic equation of the second correction for the solution of $\delta h'^{,n}$ becomes

$$A\delta h'^{,n} = \sum_{\nu=0}^{\nu_M} (\mu_\nu f_{\mathrm{IMP}}^{\delta h',(\nu)} + (1-\mu_\nu) f_{\mathrm{BDF2}}^{\delta h',(\nu)}), \tag{35}$$

which also involves a scale-dependent right-hand side. The momentum at the new time level is then computed according to

$$(h\boldsymbol{u})^{n+1} = \sum_{\nu=0}^{\nu_M} (\mu_\nu (h\boldsymbol{u})_{\mathrm{IMP}}^{n+1,(\nu)} + (1-\mu_\nu)(h\boldsymbol{u})_{\mathrm{BDF2}}^{n+1,(\nu)}), \tag{36}$$

where the scale-dependent contributions are computed by blending the updates that would be obtained by either the implicit midpoint or the BDF(2) time discretization. They are given by projecting

$$(h\boldsymbol{u})_{\mathrm{IMP}}^{n+1} = (h\boldsymbol{u})_{\mathrm{IMP}}^{**} - \frac{\Delta t}{2}(\delta h^n \nabla h'^{,n} + h^{n+1/2}\nabla \delta h'^{,n}) \tag{37}$$

and

$$(h\boldsymbol{u})_{\mathrm{BDF2}}^{n+1} = (h\boldsymbol{u})_{\mathrm{BDF2}}^{**} - \frac{2\Delta t}{3}(\delta h^n \nabla h'^{,n} + h^{n+1}\nabla \delta h'^{,n}) \tag{38}$$

to each scale using the projections from (29).

It remains to define how the blending weights for each grid level are determined. As described above, we would like to apply the implicit midpoint rule for scale components, which are well resolved by the discretization. For smaller scales the blending should be shifted successively to the BDF(2) scheme. Since the numerical dispersion heavily depends on the CFL number, in an initial attempt the blending parameter is set to be a function of the grid CFL number. For simplicity, the gravity wave speed $c = \sqrt{h}/\mathrm{Fr}$ is estimated by the square root of the mean height divided by the global Froude number in the conducted numerical simulations. This means that the grid CFL number is given by $\mathrm{cfl}_\nu = c\Delta t/\Delta x_\nu$, where Δx_ν is the grid spacing on the respective grid level ν. The blending parameter is then computed according to

$$\mu_\nu = \begin{cases} \min(1, (\nu_M - \nu)/\lfloor \log_2 \mathrm{cfl} \rfloor) & \text{if } \mathrm{cfl} \geq 2, \\ 1 & \text{otherwise,} \end{cases} \tag{39}$$

where $\lfloor \cdot \rfloor$ means rounding towards minus infinity. Thus, μ_ν is chosen such that the scheme associates the implicit midpoint discretization with all gravity wave modes corresponding to coarse grids with grid CFL number $\mathrm{cfl}_\nu \leq 1$ ($\mu_\nu = 1$), while the discretization is nudged towards BDF(2) for modes living on grids with $\mathrm{cfl}_\nu > 1$ ($\mu_\nu < 1$). However, if the fine-grid CFL number is smaller than 2, the scheme would consequently end up with using only the implicit midpoint rule. This choice of blending weights has been also used in the linear case [43].

To summarize the time advancement of the multiscale method, we outline the steps of the algorithm in the following box with a reference to the particular equations.

Semi-implicit multiscale method

(1) Explicit predictor solving the auxiliary system (10) over one time step.

(2) Solution of elliptic problem (15) for $\delta h_{\mathrm{fl}}^{\prime,n}$ to compute the advective flux correction (14).

(3) Computation of intermediate momentum updates for implicit midpoint (16) and BDF(2) discretization (20).

(4) Computation of RHS for second correction via (30)–(31) and their scale-dependent blending using μ_ν.

(5) Solution for $\delta h^{\prime,n}$ by elliptic multiscale problem (35).

(6) Computation of full momentum updates (37)–(38) and their scale-dependent blending (36) to obtain the momentum at the new time level.

3.4. ***Space discretization.*** The space discretization for the semi-implicit method is essentially the same as in the zero Froude number projection method. The major differences are that for nonzero Froude numbers two Helmholtz problems must be

solved instead of Poisson-type problems and that some care needs to be taken in order to get conservation of momentum for constant bottom topography.

The scheme is solved in one space dimension with grid cells $V_i = [x_{i-1/2}, x_{i+1/2}]$. Furthermore, a dual discretization is introduced, where each dual grid cell $\overline{V}_{i+1/2} = [x_i, x_{i+1}]$ is centered around a node $x_{i+1/2}$ of the primary grid. The whole method is discretized as a finite volume method, which has the form

$$\boldsymbol{U}_i^{n+1} = \boldsymbol{U}_i^n - \frac{\Delta t}{|V_i|}(\boldsymbol{F}_{i+1/2}^{n+1/2} - \boldsymbol{F}_{i-1/2}^{n+1/2}) + \Delta t \boldsymbol{N}_i^{n+1/2}. \tag{40}$$

Here, $|V_i|$ is the volume of cell V_i. $\boldsymbol{U}_i^n$ represents an approximation to the cell mean of the unknowns $(h, hu)^T$ in the cell V_i at time t^n, and $\boldsymbol{F}_{i+1/2}^{n+1/2}$ is the advective part of the numerical flux across the interface at $x_{i+1/2}$. The latter approximates the average of the advective flux contribution $(hu, hu^2)^T$ over one time step $[t^n, t^{n+1}]$. The additional nonconservative part $\boldsymbol{N}_i^{n+1/2}$ accounts for the gradient in surface elevation and is an approximation to $(0, -hh'_x)^T$. The equations are discretized to obtain a scheme which is in conservation form for the height equation. Conservation of momentum is only valid when no bottom topography is present. In this case, momentum should also be conserved on the discrete level. Following the above (semidiscrete) derivation of the scheme, the numerical fluxes are computed in three steps

$$\begin{aligned} \boldsymbol{F}_{i+1/2}^{n+1/2} &:= \boldsymbol{F}_{i+1/2}^{*} + \boldsymbol{F}_{i+1/2}^{\mathsf{MAC}} + 0, \\ \boldsymbol{N}_i^{n+1/2} &:= \boldsymbol{N}_i^{*} \quad + 0 \quad + \boldsymbol{N}_i^{\mathsf{P2}}, \end{aligned} \tag{41}$$

which represent contributions from the predictor and the first and second corrections, respectively. Note that the first correction only modifies the advective flux components, while the second correction only modifies the nonconservative part. The detailed contributions are given in the Appendix. For the discretization of the bottom topography b, a piecewise linear distribution on each primary grid cell which is continuous across the interfaces is assumed. The time derivatives $b_t^{n+1/2}$ are approximated by the midpoint rule using the values at full time levels.

In the predictor step the auxiliary system (10) is solved using a Godunov-type method for hyperbolic conservation laws [40]. As mentioned above, these are the pressureless equations with the "source term" $(0, -h^n h'^{,n}_x)^T$ in the momentum equation. Note that this term involves not only the contributions from the bottom topography, but also the nonconvective part of the flux function. For the integration, a semidiscretization in space with second-order reconstruction in the primitive variables and Runge–Kutta time stepping is used [33]. In particular, Heun's method is applied, which is strong stability preserving (SSP) [35; 13]. The numerical fluxes are evaluated by solving the exact Riemann problem of the pressureless equations at the cell interfaces.

In the first correction, the flux divergence of the auxiliary system is corrected, which is similar to a MAC-type projection [14; 44] in the case of the zero Froude number equations. The height correction $\delta h'^{,n}_{\mathrm{fl}}$ is continuous and piecewise linear on the dual grid, which is the 1D analogue as it was used in the solution of an elliptic problem in [36], or in the first correction of the method in [42] in two space dimensions. The fluid depth h^n in the weighted Laplacian of (15) is interpolated at the nodes of the primary grid by taking the average from the two neighboring cells (cf. [21]).

For the second correction, the divergence on the right-hand side of (23) is applied to each dual control volume. This leads to a 1D divergence defined by

$$\bar{\mathsf{D}}_{i+1/2}(u) := \frac{1}{|\bar{V}_{i+1/2}|}(u_{i+1} - u_i). \tag{42}$$

Also the computed correction $\delta h'^{,n}$ is assumed to be continuous and piecewise linear, but this time on the primary cells. Moreover, it needs to be defined how the fluid depth which enters as weight in the Laplacian on the left-hand side of (23) is discretized. Here we assume that the fluid depth is piecewise constant on each cell. This leads to a piecewise constant distribution of $h(\delta h'^{,n})_x$, and the weighted Laplacian resulting from the divergence (42) is well defined.

Concerning conservation of momentum in the case of flat bottom topography, it must be ensured that the term

$$hh'_x = h_0 h'_x + \mathsf{Fr}^2 h' h'_x \tag{43}$$

in the momentum equation can be written as a divergence on the discrete level. Since h_0 is constant in this case, this is no problem for the first term on the right-hand side of (43). For the second term, the equality

$$h' h'_x = \tfrac{1}{2}((h')^2)_x \tag{44}$$

has to be achieved on the discrete level. We realize this by taking

$$(h' h'_x)_i = \left(\frac{h'_{i+1/2} + h'_{i-1/2}}{2}\right)\left(\frac{h'_{i+1/2} - h'_{i-1/2}}{\Delta x}\right) = \frac{(h'_{i+1/2})^2 - (h'_{i-1/2})^2}{2\Delta x}, \tag{45}$$

where the interface values are linearly interpolated from cell mean values.

The spatial discretization of the scale splitting in the second correction of the multiscale scheme is obtained by eliminating every second grid node or, equivalently, by merging two adjacent cells. In this setup the restriction and prolongation operators used in standard multigrid algorithms can be utilized to define the space decomposition. Here we use full weighting (restriction) and linear interpolation (prolongation) [37] for the fluid depth, which can be defined by a stencil. The full

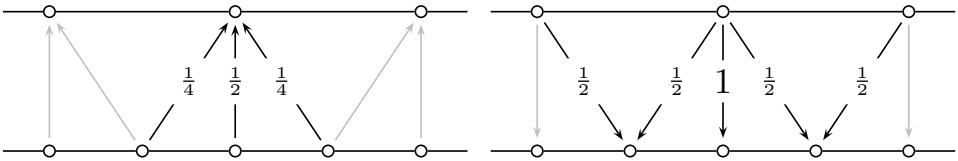

Figure 1. One-dimensional versions of full weighting (left) and linear interpolation (right) operators known from standard finite difference geometric multigrid. Arrows indicate mappings between grid functions associated with grid nodes.

weighting is given by

$$R^{(\nu)} = \tfrac{1}{4}\begin{bmatrix}1 & 2 & 1\end{bmatrix}, \tag{46}$$

which means that a variable on the coarse grid node at grid level (ν) is derived by averaging over the values at the same node and the two adjacent nodes on the fine grid at grid level $(\nu+1)$ with the weights given in the stencil above (see also Figure 1, left). The linear interpolation from grid level (ν) to grid level $(\nu+1)$ is given by

$$P^{(\nu)} = \tfrac{1}{2}\begin{bmatrix}1 & 2 & 1\end{bmatrix}. \tag{47}$$

This means that the heights at grid nodes living on the fine grid level, which have a common coarse grid node, obtain the same values as on the coarse grid. The values at grid nodes in between are computed by the average of the values of the adjacent grid nodes (Figure 1, right). Note that $P^{(\nu)}$ and $R^{(\nu)}$ are adjoint up to a scaling factor.

Since $\delta h'$ and $(h\boldsymbol{u})$ are staggered in space, the splitting in the momentum field cannot be the same as the one for the height update. Ideally, the splitting should be chosen such that only the portion of the height update associated with the grid level (ν) enters the update for the momentum on the same grid level. Revisiting equations (37) and (38) shows that only first derivatives of $\delta h'$ at different time levels enter the momentum update. Therefore, the splitting in the momentum must match the splitting in $\partial\delta h'/\partial x$ induced by the h-splitting [43]. This results in a restriction with stencil

$$\widehat{R}^{(\nu)} = \tfrac{1}{8}\begin{bmatrix}1 & 3 & 3 & 1\end{bmatrix} \tag{48}$$

for the momentum (Figure 2, left). The obvious choice for the prolongation operator is a scaled version of the adjoint of the restriction operator $\widehat{R}^{(\nu)}$, which results in

$$\widehat{P}^{(\nu)} = \tfrac{1}{4}\begin{bmatrix}1 & 3 & 3 & 1\end{bmatrix}, \tag{49}$$

which is visualized in Figure 2, right.

A grid function φ can then be decomposed into fractions $\varphi^{(\nu)}$ associated to different grid levels using the prolongation and restriction operators $P^{(\nu)}$ and $R^{(\nu)}$.

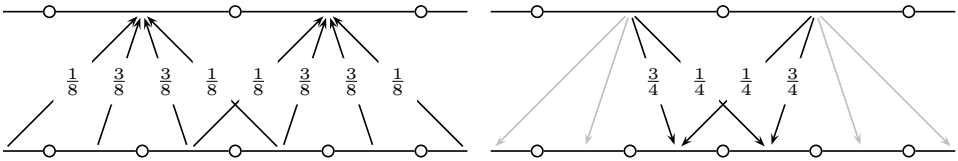

Figure 2. One-dimensional versions of restriction (left) and prolongation (right) operators for the momentum variable. Arrows indicate mappings between grid functions associated with grid cells (instead of with grid nodes as in Figure 1).

The grid function on the coarsest level is obtained by the operation

$$\varphi^{(0)} = (R^{(0)} \circ R^{(1)} \circ \cdots \circ R^{(\nu_M - 1)})\varphi, \tag{50}$$

and the grid functions on finer levels are computed by

$$\varphi^{(\nu)} = (I - P^{(\nu-1)} \circ R^{(\nu-1)}) \circ (R^{(\nu)} \circ R^{(\nu+1)} \circ \cdots \circ R^{(\nu_M - 1)})\varphi. \tag{51}$$

An application of the multiscale Helmholtz operator is then realized by decomposing the data into scales, scale-dependent weighting, and rebuilding the full variable. This gives the diagonal component of the operator, which includes the multiscale information. The Laplacian part can just be computed on the finest grid level, since it does not include any multiscale information.

4. Numerical results

Having derived the multiscale scheme for computing low Froude number shallow water flows, in this section the performance of the method is evaluated for some test cases. Besides the goal of numerically verifying the second-order accuracy of the method, its asymptotic behavior in the low Froude number regime as described in Section 2.2 is investigated.

The results of the multiscale method are compared to those obtained with the semi-implicit method using the implicit midpoint rule and the BDF(2) discretization in the second correction. With the exception of the last test case, the computations for the BDF(2) and the multiscale schemes are always started with an initial first step by the implicit midpoint rule. With this, enough old time step values can be provided for the BDF(2)-based scheme. As mentioned above, the blending parameter μ_ν in the multilevel scheme is computed according to (39). However, the precise values are always given for reference in each test case.

Since the presented scheme is semi-implicit, two Courant numbers [6] are considered. The Courant number concerning the maximum propagation speed of information is essentially associated with the propagation of gravity waves in the low Froude number case and denoted by $\mathrm{cfl}_{\mathrm{grav}}$. Furthermore, the Courant number concerning advective phenomena (which are mainly computed by the

explicit predictor) is given by $\mathrm{cfl}_{\mathrm{adv}} := \max_i(|u_i|)\Delta t/\Delta x$, where u_i is the velocity computed for each cell.

The linear systems for the solution of $\delta h'^{,n}_{\mathrm{fl}}$ and $\delta h'^{,n}$ are solved using a matrix-free implementation of the Bi-CGSTAB algorithm [39]. In each iteration, the Euclidean norm of the residual vector is calculated, and the algorithm is terminated when either the absolute value or the value relative to the norm of the initial residuum is less than a given tolerance. In the presented calculations, this tolerance is set to 10^{-10}.

4.1. ***Weakly nonlinear gravity wave.*** The first test case is set up with data, which consists of an initially smooth right-running shallow water simple wave in one space dimension with flat bottom topography. Due to the nonlinearity of the governing equations, a shock develops after some time. While this is one of the most simple setups one can think of, it already reveals some interesting properties of the considered numerical schemes: by the use of the method of characteristics, the exact solution is known until the development of a shock, which is useful for a convergence study. The behavior of the different schemes towards the compressible regime can also be tested, when the exact solution eventually develops a shock. Furthermore, the evolution of long-wave gravity waves can be analyzed, which is relevant for the asymptotic regime described in Section 2.2 and similar to what was investigated for the linearized equations (cf. [43; 41]).

To derive the initial conditions, let us consider the characteristic variables of the shallow water equations. These are given by (see, e.g., [11])

$$p_1 = u - 2c \quad \text{and} \quad p_2 = u + 2c, \tag{52}$$

where $c = \sqrt{h}/\mathsf{Fr}$ is the gravity wave speed. The definition of a background state $h_0 = 1$ leads to $c_0 = 1/\mathsf{Fr}$. Then, the initial gravity wave speed is given by

$$c = c_0 + c' = \frac{1}{\mathsf{Fr}} + c'. \tag{53}$$

To obtain a right-running simple wave, the left-running characteristic is set to $p_1 = \text{const}$. This constant is chosen to obtain a zero background flow, i.e., $p_1 = -2c_0$, which gives the initial velocity field

$$u = 2(c - c_0) = 2c'. \tag{54}$$

Therefore, initially the local Froude number ranges from 0 to $\mathsf{Fr}_{\max} \approx u_{\max}/c_0 = 2\mathsf{Fr}\max_{x\in\Omega}(c'(x))$. For the performed simulations the perturbation of the gravity wave speed is set to $c'(x) = \frac{1}{2}\sin(2\pi x)$. The computational domain is defined by the interval $\Omega = [0, 1]$ with 256 grid cells and periodic boundary conditions.

In a first setup, the Froude number is set to $\mathsf{Fr} = 0.1$ and the time step is chosen to be $\Delta t = 0.003$, which is equivalent to initial Courant numbers $\mathrm{cfl}_{\mathrm{adv}} \approx 0.77$

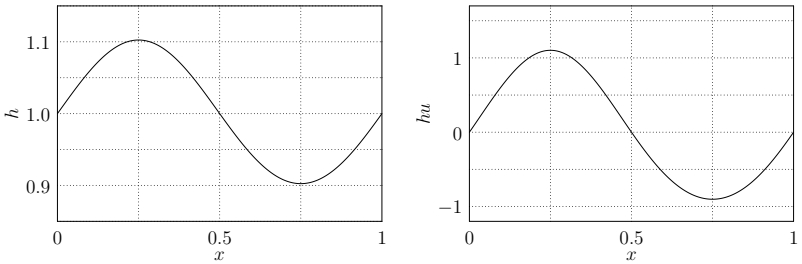

Figure 3. Initial conditions for the weakly nonlinear gravity wave test case with $\mathsf{Fr} = 0.1$ on a grid with 256 grid cells. Left: fluid depth. Right: momentum.

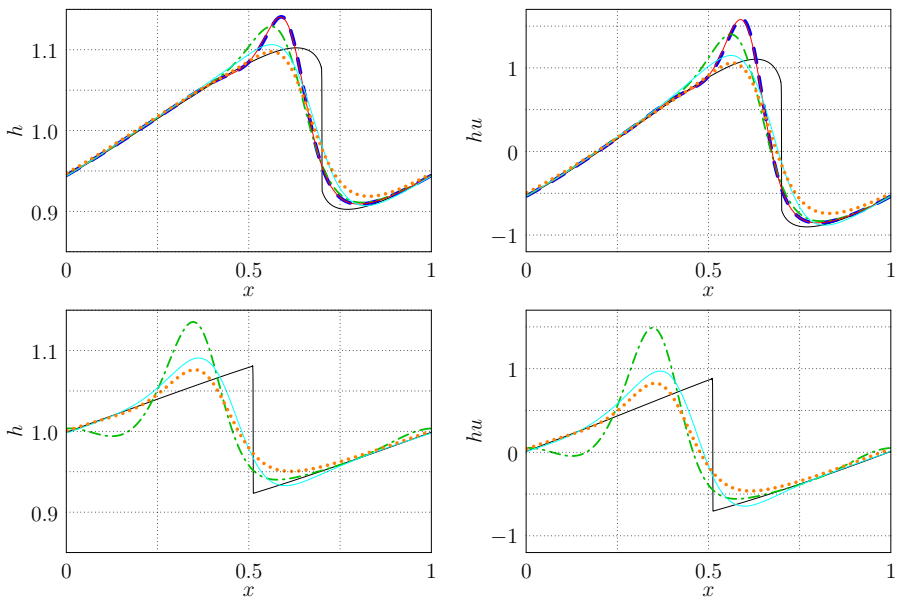

Figure 4. Solution of the weakly nonlinear gravity wave test case with $\mathsf{Fr} = 0.1$ at times $t = 0.12$ (top) and $t = 0.3$ (bottom) computed with $\mathrm{cfl}_{\mathrm{grav}} \approx 8.83$ on a grid with 256 grid cells. Black: exact solution. Blue dashed: implicit midpoint rule. Green dash-dotted: BDF(2)-type discretization. Orange dotted: off-centered scheme ($\theta = 0.7$). Red: multiscale implicit midpoint/BDF(2) scheme. Cyan: multiscale implicit midpoint/implicit Euler scheme. Note that the implicit midpoint rule and the multiscale implicit midpoint/BDF(2) schemes are only shown for $t = 0.12$.

concerning advection and $\mathrm{cfl}_{\mathrm{grav}} \approx 8.83$ concerning the propagation of gravity waves. In Figure 3 the initial conditions for fluid depth and momentum are given. The solutions of the numerical schemes are given after 40 ($t = 0.12$) and 100 time steps ($t = 0.3$) in Figure 4. At these times the wave has traveled approximately 1.2 and 3 times, respectively, through the domain. Since a shock forms at time $t_{\mathrm{shock}} = 1/(3\pi)$, this test shows the performance of the schemes towards the compressible

regime. The multiscale scheme is set up with three grid levels and blending factors $\mu_{\boldsymbol{\nu}} = (1, \frac{1}{2}, 0)$.

In addition we present results for the θ-scheme with $\theta = 0.7$ and another variant of the multiscale scheme where we switch between the implicit midpoint rule and the implicit Euler method (θ-scheme with $\theta = 1$). For the latter we choose six grid levels with blending factors $\mu_{\boldsymbol{\nu}} = (1, \frac{1}{2}, 0, 0, 0, 0)$. Note that this choice is different from what one would obtain using (39).

As one can see in Figure 4, for $t = 0.12$ the implicit midpoint rule and multiscale scheme develop an artificial overshot in the vicinity of the shock, which continuously grows until either the time step has to be reduced or the schemes become unstable (which already happens before the time $t = 0.3$). Since the initial data only consists of long-wave information, and the contributions on the smaller scales are only small corrections, the results for both schemes are almost identical. On the other hand, the θ-scheme does not show this behavior, and the discontinuity is smeared out by numerical diffusion. The BDF(2)-based scheme shows a behavior which is in between these two extrema. To show that the multiscale scheme can also be used to suppress the spurious overshot, we have implemented the version of the multiscale scheme where we switch between the implicit midpoint rule and the implicit Euler. In this case, high wavenumbers are diffused by the first-order method, while the long-wave components are preserved.

The described behavior becomes even more evident at the later time $t = 0.3$, where we only show the BDF(2), the θ-scheme, and the multiscale implicit midpoint/implicit Euler scheme, due to the stability problem of the implicit midpoint rule. Additionally, all schemes introduce a dispersive error in that they slow down the speed of the simple wave.

To test the evolution of long-wave gravity waves, the Froude number is reduced to $\mathsf{Fr} = 0.02$ in a second setup. This further decreases the nonlinearity of the equations compared to the case with $\mathsf{Fr} = 0.1$. However, due to the configuration of the initial data, the shock develops at the same time $t_{\text{shock}} = 1/(3\pi)$ as before. The initial conditions for this test case are shown in Figure 5, top. The time step is again $\Delta t = 0.003$, which is equivalent to initial Courant numbers $\text{cfl}_{\text{adv}} \approx 0.77$ and $\text{cfl}_{\text{grav}} \approx 39.55$. The solution at time $t = 0.024$ is displayed in Figure 5, bottom. At this time, the gravity wave has traveled approximately 1.2 times through the domain, and its shape has not yet been distorted much compared to the initial data. For this test, the multiscale scheme is applied with six levels and blending parameters $\mu_{\boldsymbol{\nu}} = (1, \frac{4}{5}, \frac{3}{5}, \frac{2}{5}, \frac{1}{5}, 0)$.

At the final time the implicit midpoint rule and the multiscale scheme show the smallest error in amplitude and phase compared to the exact solution. Also in this case the solutions of these schemes are nearly identical. The worst results are produced by the off-centered scheme, which has the biggest phase and amplitude

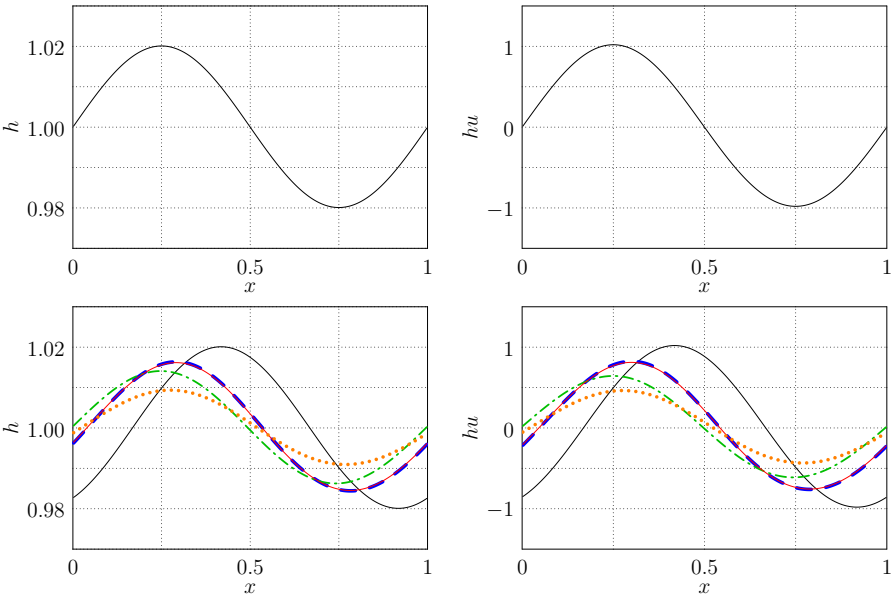

Figure 5. Weakly nonlinear gravity wave test case with $\mathsf{Fr} = 0.02$ computed with $\mathrm{cfl}_{\mathrm{grav}} \approx 39.55$ on a grid with 256 grid cells. Top: initial conditions. Bottom: solution at $t = 0.024$. Black: exact solution. Blue dashed: implicit midpoint rule. Green dash-dotted: BDF(2)-type discretization. Orange dotted: off-centered scheme ($\theta = 0.7$). Red: multiscale scheme.

errors. The method with BDF(2) in the second correction produces results which are in between these two extrema.

4.2. ***Convergence in one space dimension.*** The same initial conditions of a right-running gravity simple wave and for $\mathsf{Fr} = 0.1$ are used in order to undertake a convergence analysis. The solution of the numerical schemes is computed on different grids and compared to the exact solution at time $t_{\mathrm{end}} = 0.05$. At this time no shock has developed yet, and the true solution can be computed using the method of characteristics. The numerical solution is computed on grids with 256, 512, 1024, and 2048 cells, and the respective time steps are given by $\Delta t_{256} = \frac{1}{320}$, $\Delta t_{512} = \frac{1}{640}$, $\Delta t_{1024} = \frac{1}{1280}$, and $\Delta t_{2048} = \frac{1}{2560}$. This corresponds to an advective Courant number $\mathrm{cfl}_{\mathrm{adv}} = 0.8$. For the multiscale method, five grid levels with $\mu_{\boldsymbol{\nu}} = (1, 1, \frac{2}{3}, \frac{1}{3}, 0)$ are used.

For the computation of errors and the convergence rate, the error vectors $\boldsymbol{e}^N$ in fluid depth and momentum are calculated. For the latter it has elements

$$e_i^N := (hu)_i(t_N) - (hu)_i^N \tag{55}$$

where the cell mean values of the exact solution are compared with those of the simulated data. The global error is measured using discrete versions of the L^2 and

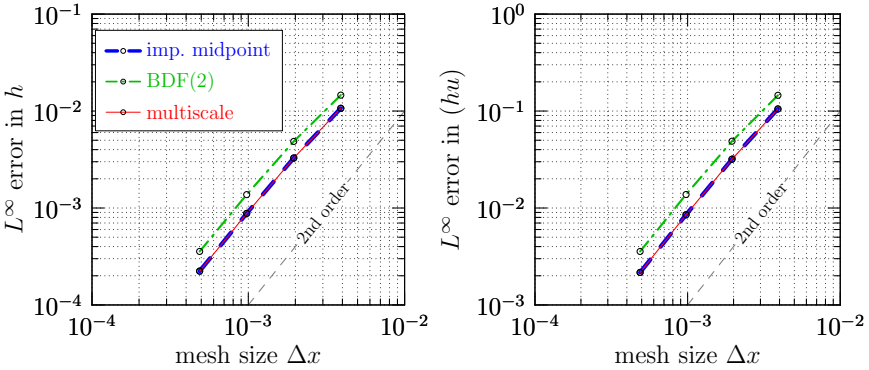

Figure 6. Convergence for the one-dimensional simple wave test case. L^∞ errors in h and (hu) for the different variants of the semi-implicit method.

the L^∞ norms. These are defined by

$$\|\boldsymbol{e}^N\|[2] := \left(\sum_i |V_i||e_i^N|^2\right)^{1/2} \quad \text{and} \quad \|\boldsymbol{e}^N\|[\infty] := \max_i\{e_i^N\}. \tag{56}$$

The experimental convergence rate γ is calculated by the formula

$$\gamma := \frac{\log(\|\boldsymbol{e}_c^N\|/\|\boldsymbol{e}_f^N\|)}{\log(\Delta x_c/\Delta x_f)}. \tag{57}$$

In this definition, $\boldsymbol{e}_c^N$ and $\boldsymbol{e}_f^N$ are the computed error vectors of the solution on a coarse and a fine grid and Δx_c and Δx_f are the corresponding grid spacings.

The error of the numerical solutions in the L^∞ norm is summarized in Figure 6. Furthermore, the precise values in the L^2 and L^∞ norms are given in the Appendix in Tables 1 and 2, where also the convergence rates γ between the grid levels are calculated. On fixed grids, the scheme with implicit midpoint discretization in the second correction produces the smallest errors. The method with a BDF(2)-based second correction produces errors which are about 1.5 times larger. The multiscale scheme produces errors which are comparable with those from the implicit midpoint rule. This is again due to the long-wave nature of the initial conditions. As given by the values of μ_ν, only the finest scales of the BDF(2)-based method are applied, which means that the calculations are nearly identical up to small deviations. The experimental convergence rates suggest for all schemes second-order accuracy.

4.3. ***Balanced modes in presence of time-dependent bottom topography.*** In a final test case, the schemes are tested for their ability to relax to nontrivial balanced states in the presence of bottom topography varying in time. In order to do so, a test case from [43] (see also [41]) for the linearized equations is extended to the fully nonlinear shallow water equations. The test is defined in one space dimension

on the domain $\Omega = [0, 100]$. The bottom topography is given by

$$b(t, x) = \frac{\mathsf{Fr}}{\omega} \sin(\omega t)\tilde{q}(x - x_0), \tag{58}$$

where

$$\tilde{q}(x) = \left[\frac{2\sigma^2 + \lambda^2\sigma^4 - 4x^2}{\lambda^2\sigma^4} \sin(\lambda x) + \frac{4x}{\lambda\sigma^2} \cos(\lambda x)\right] \exp\left(-\left(\frac{x}{\sigma}\right)^2\right). \tag{59}$$

This means that the term $b_t(t, x) = \mathsf{Fr} \cos(\omega t)\tilde{q}(x - x_0)$ must be balanced by the production of local divergence. The parameters are given by $\omega = 0.2\pi$, $x_0 = 50$, $\sigma = 10$, and $\lambda = 0.32\pi$. Initially the fluid is at rest ($u \equiv 0$) with fluid depth $h \equiv 1$. When the flow is in balance, the findings from Section 2 imply that for small Froude numbers the perturbations in fluid depth and momentum should also be small, and the dynamics primarily happen in the linear regime. This means that the solution is essentially governed by the asymptotic solution obtained for the linearized shallow water equations. Translated to the given initial value problem and bottom topography, the asymptotic solutions of the perturbation in fluid depth and the velocity are

$$H_{\text{asy}}(t, x) - H_0 = -\frac{\mathsf{Fr}^3}{H_0} \omega \sin(\omega t)\tilde{h}(x - x_0) \tag{60}$$

with $\tilde{h}(x) = \lambda^{-2} \sin(\lambda x) \exp(-(x/\sigma)^2)$, and

$$u_{\text{asy}}(t, x) = \frac{\mathsf{Fr}}{H_0} \cos(\omega t)\tilde{u}(x - x_0), \tag{61}$$

where $\tilde{u}(x) = [2x(\sigma\lambda)^{-2} \sin(\lambda x) - \lambda^{-1} \cos(\lambda x)] \exp(-(x/\sigma)^2)$.

In the presented computations, the Froude number is set to $\mathsf{Fr} = 0.01$ and the total background height is $H_0 = 1$. The computational grid has 256 grid cells, and the fixed time step is given by $\Delta t = 0.24$, which corresponds to an advective Courant number $\text{cfl}_{\text{adv}} \approx 0.006$ when the flow is essentially balanced. The Courant number corresponding to the transport of gravity waves is $\text{cfl}_{\text{grav}} \approx 61$.

For this test case the BDF(2)-based computations are not initialized with an initial step by the implicit midpoint rule. Instead, the required state at $t^{-1} = -0.24$ is set to the balanced solution with flat bottom topography. However, compared to an initialization using the implicit midpoint rule, the findings are qualitatively the same. For the multiscale method six grid levels are used with a scale-dependent blending given by $\mu_\nu = (1, \frac{4}{5}, \frac{3}{5}, \frac{2}{5}, \frac{1}{5}, 0)$.

Given the above initial conditions for $t = 0$, the fluid depth is in balance with the initial bottom topography. However, the temporal change of the latter introduces divergence into the velocity field, which, in turn, results in higher-order perturbations in the fluid depth. In Figure 7, the numerical results are displayed together with

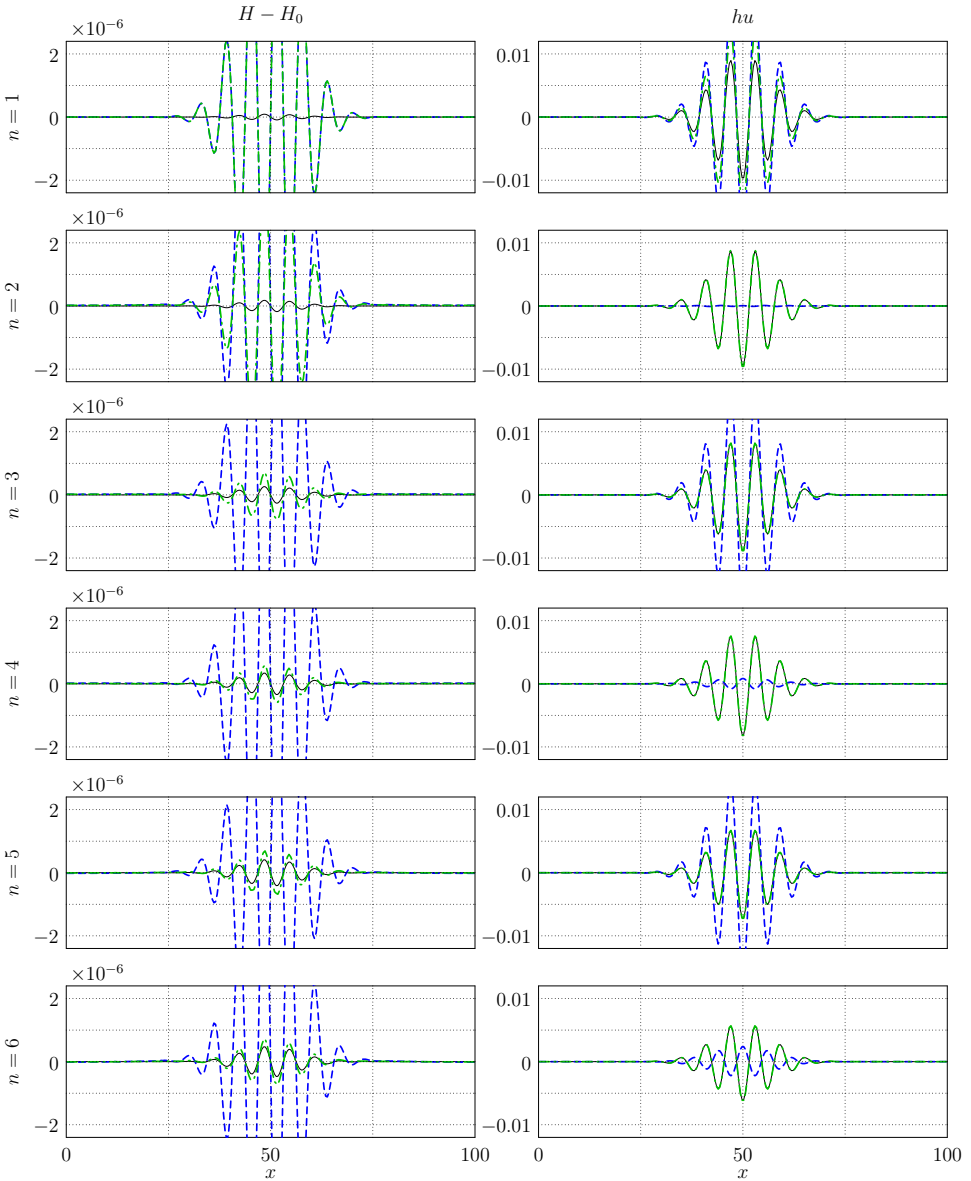

Figure 7. Numerical solution of the balancing test case after the first six time steps using the implicit midpoint rule (blue dashed) and the BDF(2) scheme (green dash-dotted) on a grid with 256 cells and $\mathsf{Fr} = 0.01$. Left column: perturbation in fluid depth. Right column: momentum. Each step n is one row. The asymptotic solution is plotted as a black line.

the asymptotic solution for the first six time steps using the implicit midpoint rule and BDF(2)-based discretization. Using the implicit midpoint rule, both the computed perturbations in the fluid depth and the momentum field oscillate around

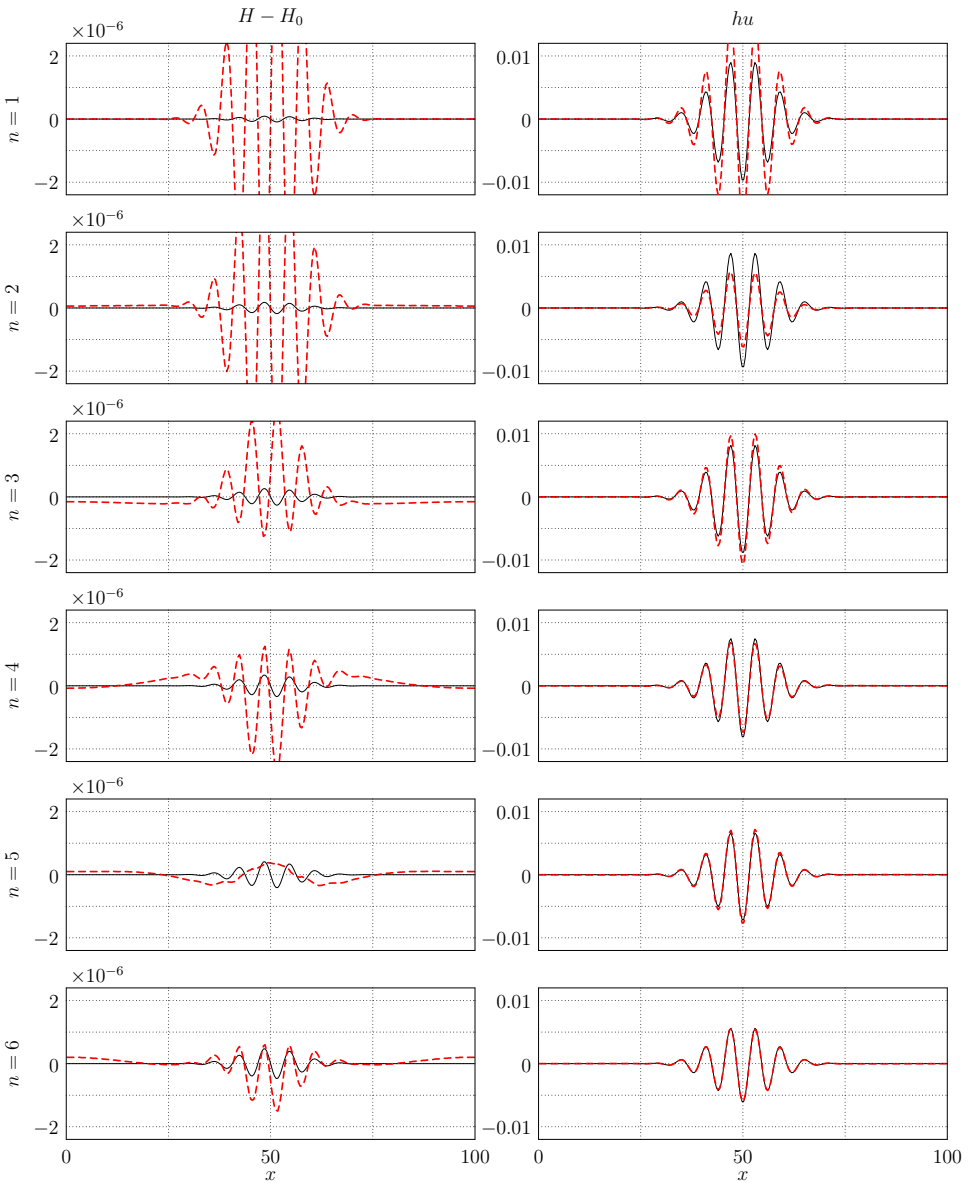

Figure 8. Same as Figure 7, but using the multiscale scheme (red dashed).

the balanced state, but they do not relax to it. Additionally, the amplitude of the numerically calculated perturbations in the fluid depth are about 8 times larger compared to the asymptotic solution. The BDF(2)-based discretization results in a completely different behavior. Here, the initial deviations from the balanced state vanish after only a few time steps. After the fourth time step the numerical solution

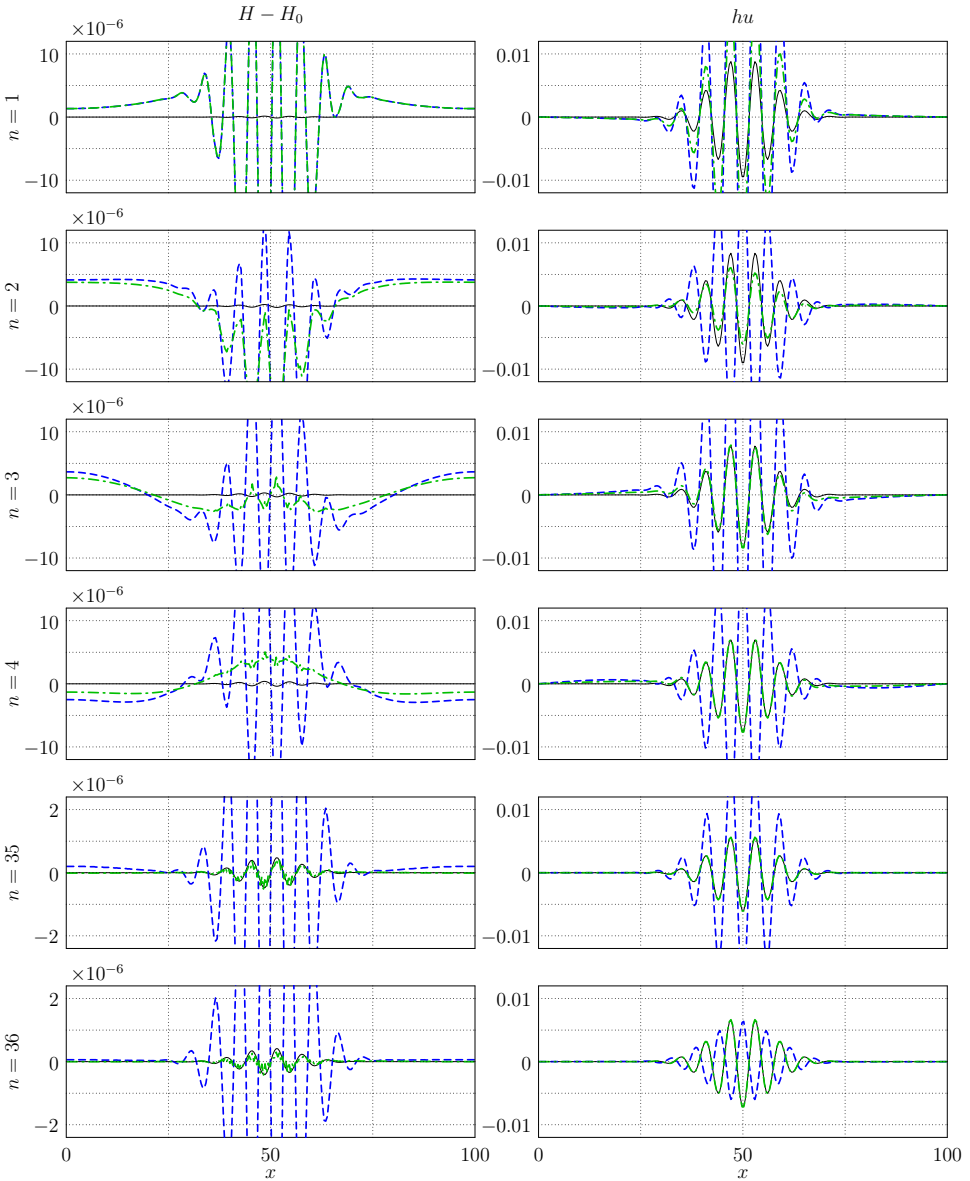

Figure 9. Numerical solution of the balancing test case using completely unbalanced initial data after the first 4 time steps and time steps 35 and 36 using the implicit midpoint rule (blue dashed) and the BDF(2) discretization (green dash-dotted) on a grid with 256 cells and $\mathsf{Fr} = 0.01$. The asymptotic solution is plotted as a black line.

is nearly indistinguishable from the asymptotic solution. This behavior is also reproduced by the multiscale method, for which the results are given in Figure 8.

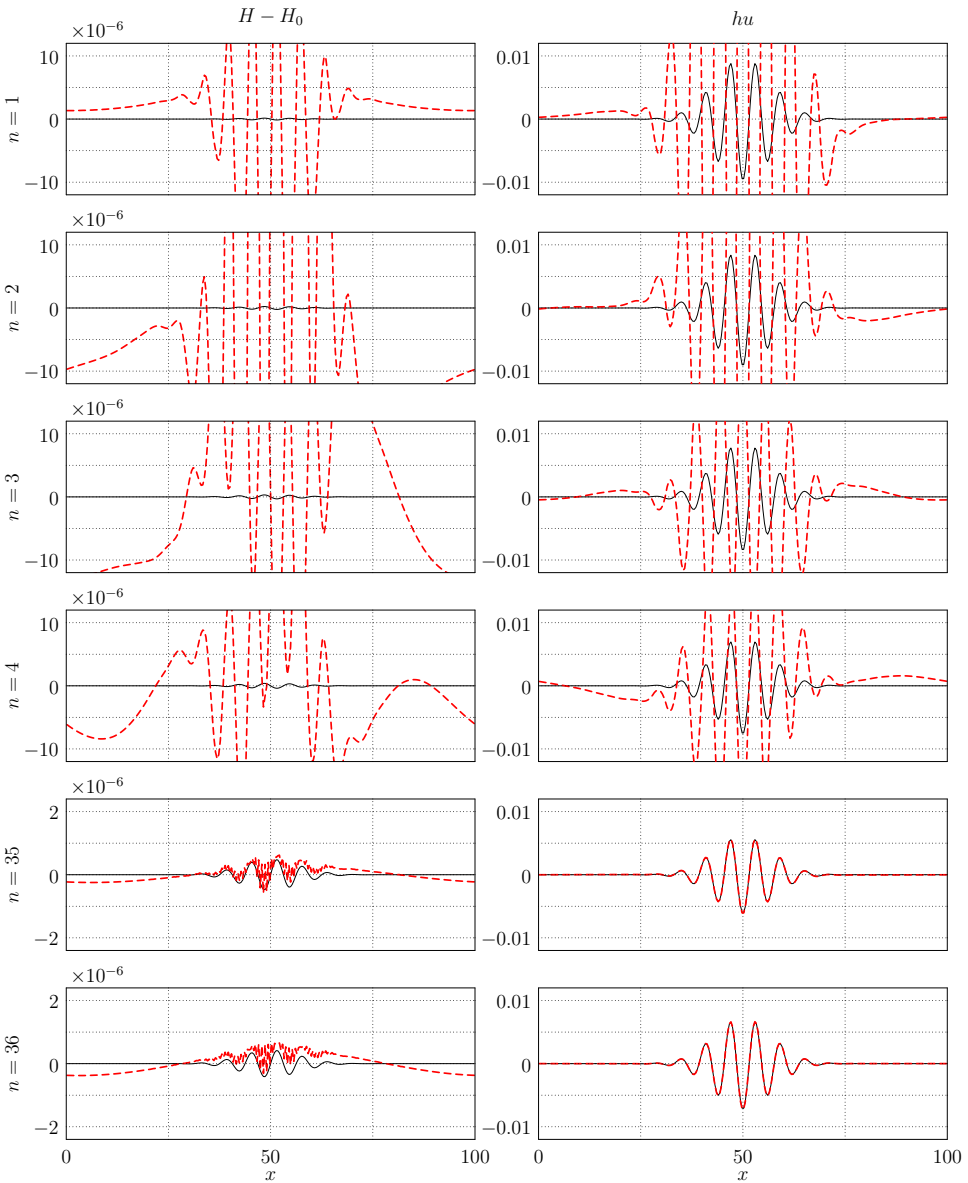

Figure 10. Same as Figure 9, but using the multiscale scheme (red dashed).

These results are in good agreement with the findings for the linearized shallow water equations [43; 41].

In a second run, the simulation is started at $t = 0.15$, and the bottom topography is assumed to be flat before this time. At this time, when the bottom topography switches instantaneously to another state, both fluid depth and momentum are not in

balance. This leads to much bigger initial deviations from the asymptotic solution, as can be seen in Figure 9 for the implicit midpoint rule and the BDF(2)-type discretization (note the different scaling in the y-axis for the perturbation in fluid depth for the first four time steps). To evaluate the long-term behavior, the numerical solution is additionally plotted for the time steps 35 and 36. Also in this case the solution of the implicit midpoint rule does not relax to the balanced state, but rather oscillates around it. Only the long-wave perturbations are diminished with time. Here, the perturbations in fluid depth computed by the numerical scheme are about two orders of magnitude larger than those predicted by the asymptotic solution. For the momentum, the amplitude of the numerical solution is also about three times larger than the predicted balanced state.

The BDF(2)-based method, on the other hand, shows a behavior similar to the first setup. After initial deviations, which are of the same order as for the implicit midpoint rule, the numerical solutions essentially relax to the balanced state predicted by the asymptotic solution. Only in the fluid depth, very high-wave-number small-amplitude deviations persist. Additional tests (not shown) suggest that these artifacts are due to the fact that the explicit predictor cannot cope with too high-wave-number modes at these large Courant numbers. In this part of the scheme, a two-stage Runge–Kutta method is used for the time discretization. Since the gravity waves are generated by the "source term" of the predictor, which is always evaluated at the old time level, high-wave-number gravity waves get very much distorted in the second stage of the Runge–Kutta scheme. This can eventually lead to instabilities, if these parts of the solution become to large.

The results of the multiscale method are given in Figure 10. Qualitatively, the behavior is similar to the BDF(2)-based second correction. However, the scale-dependent blending of the two methods leads to even larger very high-wave-number deviations, but whose amplitude is of the order of the perturbations in fluid depth. Also some long-wave perturbations persist, which cannot propagate away due to the periodic boundary conditions.

5. Conclusion

In this work, a new multiscale semi-implicit method for the numerical solution of low Froude number shallow water flows is introduced. It is motivated by significant shortcomings of classical semi-implicit large time step integration schemes applied in current atmospheric codes. A principal feature of the new method is the diverse treatment of long- and short-wave solution components in accordance with the asymptotic regime of fast gravity waves traveling over short-range topography. This is achieved through a multilevel approach borrowing ideas from multigrid schemes

method	norm	256	rate γ	512	rate γ	1024	rate γ	2048
trapezoidal rule	L^2	3.2801×10^{-3}	1.846	9.1251×10^{-4}	1.955	2.3530×10^{-4}	1.991	5.9190×10^{-5}
	L^∞	1.0686×10^{-2}	1.705	3.2770×10^{-3}	1.898	8.7942×10^{-4}	1.977	2.2342×10^{-4}
BDF(2)	L^2	4.7937×10^{-3}	1.763	1.4127×10^{-3}	1.912	3.7548×10^{-4}	1.975	9.5495×10^{-5}
	L^∞	1.4599×10^{-2}	1.587	4.8593×10^{-3}	1.822	1.3743×10^{-3}	1.947	3.5642×10^{-4}
multiscale method	L^2	3.2793×10^{-3}	1.846	9.1193×10^{-4}	1.956	2.3512×10^{-4}	1.991	5.9157×10^{-5}
	L^∞	1.0661×10^{-2}	1.703	3.2748×10^{-3}	1.898	8.7882×10^{-4}	1.977	2.2328×10^{-4}

Table 1. Errors and convergence rates in h for the different variants of the semi-implicit method.

for elliptic equations. The scheme is second-order accurate and admits time steps depending essentially on the flow velocity.

The multiscale scheme is able to properly propagate long-wave gravity waves, and their dispersion and amplitude errors are minimized as much as the considered base schemes admit. However, some artifacts can be observed in the fluid depth, which are probably related to the explicit predictor of the semi-implicit method. But these should be acceptable in practical applications. In the presence of bottom topography, which varies slowly in time, the balanced state is attained after a reasonable number of time steps.

The ultimate goal of this work is to develop a multiscale multiply blended scheme that does not only account for the scale-dependent propagation properties of the various wave modes in the atmosphere, thereby creating the numerical analogue of the blended model formulation of [23].

The source code for the method and tests are available upon request from the authors.

Appendix

A.1. ***Numerical fluxes of the finite volume scheme.*** As outlined in (41), the numerical fluxes are computed in three steps. Here, the particular terms using the trapezoidal rule in the second correction are given. The case using the BDF(2) discretization uses the same spatial operators, but has some differences in the particular terms. $\boldsymbol{F}_I^*$ and $\boldsymbol{N}_i^*$ are the numerical fluxes approximating the flux function and "source term" of the auxiliary system, respectively. These are

$$\boldsymbol{F}_I^* = \begin{pmatrix} (hu)^{n+1/2} \\ (hu)^{n+1/2} u^{n+1/2} \end{pmatrix} \quad \text{and} \quad \boldsymbol{N}_i^* = \begin{pmatrix} 0 \\ -(hh'_x)^n \end{pmatrix}. \tag{62}$$

The second flux term

$$\boldsymbol{F}_I^{\mathsf{MAC}} := -\frac{\Delta t}{2} \begin{pmatrix} h^n (\delta h'^{,n}_{\mathrm{fl}})_x \\ (hu)^{*,n+1/2} (\delta h'^{,n}_{\mathrm{fl}})_x + h^n (\delta h'^{,n}_{\mathrm{fl}})_x u^{*,n+1/2} \end{pmatrix}_I \tag{63}$$

method	norm	256	rate γ	512	rate γ	1024	rate γ	2048
trapezoidal rule	L^2	3.2422×10^{-2}	1.864	8.9047×10^{-3}	1.961	2.2875×10^{-3}	1.991	5.7556×10^{-4}
	L^∞	1.0527×10^{-1}	1.722	3.1899×10^{-2}	1.904	8.5226×10^{-3}	1.977	2.1654×10^{-3}
BDF(2)	L^2	4.7676×10^{-2}	1.740	1.4277×10^{-2}	1.910	3.8002×10^{-3}	1.976	9.6614×10^{-4}
	L^∞	1.4534×10^{-1}	1.573	4.8843×10^{-2}	1.826	1.3778×10^{-2}	1.952	3.5620×10^{-3}
multiscale method	L^2	3.2404×10^{-2}	1.865	8.8982×10^{-3}	1.961	2.2855×10^{-3}	1.990	5.7521×10^{-4}
	L^∞	1.0494×10^{-1}	1.720	3.1864×10^{-2}	1.904	8.5157×10^{-3}	1.976	2.1639×10^{-3}

Table 2. Errors and convergence rates in (hu) for the different variants of the semi-implicit method.

corresponds to the first correction computed by (15). As stated above, with this correction the new time level fluid depth can be determined. The third contribution in (41) is given by

$$N_i^{\mathrm{P2}} := \begin{pmatrix} 0 \\ -\frac{1}{2}(\delta h^n h_x'^{,n} + h^{n+1/2}\delta h_x'^{,n}) \end{pmatrix}_i \tag{64}$$

and represents the correction computed by the second Helmholtz equation (23).

A.2. ***"Simple wave" test case.*** The computed errors and convergence rates (cf. Section 4.2) are given in Tables 1 and 2.

Acknowledgements

The authors acknowledge partial support by Deutsche Forschungsgemeinschaft through the Collaborative Research Center 1114 "Scaling cascades in complex systems", Project A02, and by Einstein Stiftung Berlin through the Einstein Visiting Fellowship "Multiscale atmospheric flows: rigorous analysis, ensemble downscaling, and data assimilation" (Professor Edriss Titi). This work benefited greatly from free software products. Without these tools — such as LaTeX and the Linux operating system — a lot of tasks would not have been so easy to realize. It is our pleasure to thank all developers for their excellent products.

References

[1] P. R. Bannon, *On the anelastic approximation for a compressible atmosphere*, J. Atmos. Sci. **53** (1996), no. 23, 3618–3628.

[2] F. Bouchut, *On zero pressure gas dynamics*, Advances in kinetic theory and computing (B. Perthame, ed.), Ser. Adv. Math. Appl. Sci., no. 22, World Sci. Publ., River Edge, NJ, 1994, pp. 171–190. MR Zbl

[3] F. Bouchut, S. Jin, and X. Li, *Numerical approximations of pressureless and isothermal gas dynamics*, SIAM J. Numer. Anal. **41** (2003), no. 1, 135–158. MR Zbl

[4] D. Bresch, R. Klein, and C. Lucas, *Multiscale analyses for the shallow water equations*, Computational science and high performance computing IV (E. Krause, Y. Shokin, M. Resch, D.

Kröner, and N. Shokina, eds.), Notes Numer. Fluid Mech. Multidiscip. Des., no. 115, Springer, 2011, pp. 149–164. MR

[5] F. Cordier, P. Degond, and A. Kumbaro, *An asymptotic-preserving all-speed scheme for the Euler and Navier–Stokes equations*, J. Comput. Phys. **231** (2012), no. 17, 5685–5704. MR Zbl

[6] R. Courant, K. Friedrichs, and H. Lewy, *Über die partiellen Differenzengleichungen der mathematischen Physik*, Math. Ann. **100** (1928), no. 1, 32–74. MR Zbl

[7] T. Davies, A. Staniforth, N. Wood, and J. Thuburn, *Validity of anelastic and other equation sets as inferred from normal-mode analysis*, Q. J. Roy. Meteor. Soc. **129** (2003), no. 593, 2761–2775.

[8] P. Deuflhard and F. Bornemann, *Scientific computing with ordinary differential equations*, Texts in Applied Mathematics, no. 42, Springer, 2002. MR Zbl

[9] D. R. Durran, *Improving the anelastic approximation*, J. Atmos. Sci. **46** (1989), no. 11, 1453–1461.

[10] ———, *Numerical methods for fluid dynamics: with applications to geophysics*, 2nd ed., Texts in Applied Mathematics, no. 32, Springer, 2010. MR Zbl

[11] G. Erbes, *A semi-Lagrangian method of characteristics for the shallow-water equations*, Mon. Weather Rev. **121** (1993), no. 12, 3443–3452.

[12] K. J. Geratz, *Erweiterung eines Godunov-Typ-Verfahrens für zwei-dimensionale kompressible Strömungen auf die Fälle kleiner und verschwindender Machzahl*, Ph.D. thesis, Rheinisch-Westfälische Technische Hochschule Aachen, 1997.

[13] S. Gottlieb, C.-W. Shu, and E. Tadmor, *Strong stability-preserving high-order time discretization methods*, SIAM Rev. **43** (2001), no. 1, 89–112. MR Zbl

[14] F. H. Harlow and J. E. Welch, *Numerical calculation of time-dependent viscous incompressible flow of fluid with free surface*, Phys. Fluids **8** (1965), no. 12, 2182–2189. MR Zbl

[15] E. Kalnay, *Atmospheric modeling, data assimilation and predictability*, Cambridge University, 2002.

[16] J. Kevorkian and J. D. Cole, *Multiple scale and singular perturbation methods*, Applied Mathematical Sciences, no. 114, Springer, 1996. MR Zbl

[17] S. Klainerman and A. Majda, *Singular limits of quasilinear hyperbolic systems with large parameters and the incompressible limit of compressible fluids*, Comm. Pure Appl. Math. **34** (1981), no. 4, 481–524. MR Zbl

[18] R. Klein, *Semi-implicit extension of a Godunov-type scheme based on low Mach number asymptotics, I: One-dimensional flow*, J. Comput. Phys. **121** (1995), no. 2, 213–237. MR Zbl

[19] ———, *Asymptotic analyses for atmospheric flows and the construction of asymptotically adaptive numerical methods*, ZAMM Z. Angew. Math. Mech. **80** (2000), no. 11-12, 765–777. MR Zbl

[20] ———, *An applied mathematical view of meteorological modelling*, Applied mathematics entering the 21st century (J. M. Hill and R. Moore, eds.), SIAM, 2004, pp. 227–269. MR Zbl

[21] ———, *Asymptotics, structure, and integration of sound-proof atmospheric flow equations*, Theor. Comp. Fluid Dyn. **23** (2009), no. 3, 161–195. Zbl

[22] ———, *Scale-dependent models for atmospheric flows*, Annu. Rev. Fluid Mech. **42** (2010), 249–274. MR Zbl

[23] R. Klein and T. Benacchio, *A doubly blended model for multiscale atmospheric dynamics*, J. Atmos. Sci. **73** (2016), no. 3, 1179–1186.

[24] R. Klein, N. Botta, T. Schneider, C. D. Munz, S. Roller, A. Meister, L. Hoffmann, and T. Sonar, *Asymptotic adaptive methods for multi-scale problems in fluid mechanics*, J. Engrg. Math. **39** (2001), no. 1-4, 261–343. MR Zbl

[25] R. Klein, S. Vater, E. Paeschke, and D. Ruprecht, *Multiple scales methods in meteorology*, Asymptotic methods in fluid mechanics: survey and recent advances (H. Steinrück, ed.), CISM Courses and Lectures, no. 523, Springer, 2010, pp. 127–196. Zbl

[26] O. Le Maître, J. Levin, M. Iskandarani, and O. M. Knio, *A multiscale pressure splitting of the shallow-water equations, I: Formulation and 1D tests*, J. Comput. Phys. **166** (2001), no. 1, 116–151. MR

[27] R. J. Leveque, *The dynamics of pressureless dust clouds and delta waves*, J. Hyperbolic Differ. Equ. **1** (2004), no. 2, 315–327. MR Zbl

[28] F. B. Lipps and R. S. Hemler, *A scale analysis of deep moist convection and some related numerical calculations*, J. Atmos. Sci. **39** (1982), no. 10, 2192–2210.

[29] A. J. Majda and R. Klein, *Systematic multiscale models for the tropics*, J. Atmos. Sci. **60** (2003), no. 2, 393–408.

[30] C.-D. Munz, S. Roller, R. Klein, and K. J. Geratz, *The extension of incompressible flow solvers to the weakly compressible regime*, Comput. & Fluids **32** (2003), no. 2, 173–196. MR Zbl

[31] Y. Ogura and N. A. Phillips, *Scale analysis of deep and shallow convection in the atmosphere*, J. Atmos. Sci. **19** (1962), no. 2, 173–179.

[32] W. Ohfuchi, H. Nakamura, M. K. Yoshioka, T. Enomoto, K. Takaya, X. Peng, S. Yamane, T. Nishimura, Y. Kurihara, and K. Ninomiya, *10-km mesh meso-scale resolving simulations of the global atmosphere on the Earth Simulator: preliminary outcomes of AFES (AGCM for the Earth Simulator)*, J. Earth Simulator **1** (2004), 8–34.

[33] S. Osher, *Convergence of generalized MUSCL schemes*, SIAM J. Numer. Anal. **22** (1985), no. 5, 947–961. MR Zbl

[34] J. Pedlosky, *Geophysical fluid dynamics*, 2nd ed., Springer, 1987. Zbl

[35] C.-W. Shu and S. Osher, *Efficient implementation of essentially nonoscillatory shock-capturing schemes*, J. Comput. Phys. **77** (1988), no. 2, 439–471. MR Zbl

[36] E. Süli, *Convergence of finite volume schemes for Poisson's equation on nonuniform meshes*, SIAM J. Numer. Anal. **28** (1991), no. 5, 1419–1430. MR Zbl

[37] U. Trottenberg, C. W. Oosterlee, and A. Schüller, *Multigrid*, Academic, 2001. MR Zbl

[38] G. K. Vallis, *Atmospheric and oceanic fluid dynamics: fundamentals and large-scale circulation*, Cambridge, 2006. Zbl

[39] H. A. van der Vorst, *Bi-CGSTAB: a fast and smoothly converging variant of Bi-CG for the solution of nonsymmetric linear systems*, SIAM J. Sci. Statist. Comput. **13** (1992), no. 2, 631–644. MR Zbl

[40] B. van Leer, *Towards the ultimate conservative difference scheme, V: A second-order sequel to Godunov's method*, J. Comput. Phys. **32** (1979), no. 1, 101–136. Zbl

[41] S. Vater, *A multigrid-based multiscale numerical scheme for shallow water flows at low Froude number*, Ph.D. thesis, Freie Universität Berlin, 2013.

[42] S. Vater and R. Klein, *Stability of a Cartesian grid projection method for zero Froude number shallow water flows*, Numer. Math. **113** (2009), no. 1, 123–161. MR Zbl

[43] S. Vater, R. Klein, and O. M. Knio, *A scale-selective multilevel method for long-wave linear acoustics*, Acta Geophys. **59** (2011), no. 6, 1076–1108. Zbl

[44] J. E. Welch, F. H. Harlow, J. P. Shannon, and B. J. Daly, *The MAC method: a computing technique for solving viscous, incompressible, transient fluid-flow problems involving free surfaces*, Tech. Report LA-3425, Los Alamos Scientific Laboratory, 1965.

Received December 1, 2017. Revised June 27, 2018.

STEFAN VATER: stefan.vater@math.fu-berlin.de
Department of Mathematics and Computer Science, Freie Universität Berlin, Berlin, Germany

RUPERT KLEIN: rupert.klein@math.fu-berlin.de
Department of Mathematics and Computer Science, Freie Universität Berlin, Berlin, Germany

Communications in Applied Mathematics and Computational Science

msp.org/camcos

See inside back cover or msp.org/camcos for submission instructions.

The subscription price for 2018 is US $100/year for the electronic version, and $150/year (+$15, if shipping outside the US) for print and electronic. Subscriptions, requests for back issues from the last three years and changes of subscriber address should be sent to MSP.

Communications in Applied Mathematics and Computational Science (ISSN 2157-5452 electronic, 1559-3940 printed) at Mathematical Sciences Publishers, 798 Evans Hall #3840, c/o University of California, Berkeley, CA 94720-3840, is published continuously online. Periodical rate postage paid at Berkeley, CA 94704, and additional mailing offices.

CAMCoS peer review and production are managed by EditFLOW® from MSP.

PUBLISHED BY

mathematical sciences publishers

nonprofit scientific publishing

http://msp.org/

Communications in Applied Mathematics and Computational Science

vol. 13 no. 2 2018